


Research Paper

Absolute *V*-band magnitudes and mass-to-light ratios of Galactic globular clusters

H. Baumgardt¹, A. Sollima² and M. Hilker³

¹School of Mathematics and Physics, The University of Queensland, St. Lucia, QLD 4072, Australia, ²INAF Osservatorio Astronomico di Bologna, via Gobetti 93/3, Bologna 40129, Italy and ³European Southern Observatory, Karl-Schwarzschild-Str. 2, Garching 85748, Germany

Abstract

We have used *Hubble Space Telescope* and ground-based photometry to determine total *V*-band magnitudes and mass-to-light ratios of more than 150 Galactic globular clusters. We do this by summing up the magnitudes of their individual member stars, using colour-magnitude information, *Gaia* DR2 proper motions, and radial velocities to distinguish cluster stars from background stars. Our new magnitudes confirm literature estimates for bright clusters with $V < 8$, but can deviate by up to two magnitudes from literature values for fainter clusters. They lead to absolute mass-to-light ratios that are confined to the narrow range $1.4 < M/L_V < 2.5$, significantly smaller than what was found before. We also find a correlation between a cluster's M/L_V value and its age, in agreement with theoretical predictions. The M/L_V ratios of globular clusters are also in good agreement with those predicted by stellar isochrones, arguing against a significant amount of dark matter inside globular clusters. We finally find that, in agreement with what has been seen in M 31, the magnitude distribution of outer halo globular clusters has a tail towards faint clusters that is absent in the inner parts of the Milky Way.

Keywords: globular clusters: general – stars: luminosity function – mass function

(Received 7 August 2020; revised 18 September 2020; accepted 21 September 2020)

1. Introduction

Globular cluster systems are powerful tools to study the evolution of galaxies since they trace the major star formation episodes of their parent galaxies (Brodie & Strader 2006). Their colour and spatial distribution therefore allow to identify different stellar sub-populations, while their radial velocities can be used to determine the mass profile of galaxies (e.g. Richtler et al. 2011; Pota et al. 2015). In addition, past merger episodes of galaxies can be deduced from their globular cluster populations (Kruijssen et al. 2020).

For distant extragalactic globular clusters, one can normally only observe the integrated light of an otherwise unresolved cluster, so integrated magnitudes and broadband colours must be used to infer the mass, age, and metallicity of each cluster. In order to facilitate such studies, it is useful to know the same integrated magnitudes and colours of Milky Way globular clusters. This is due to the fact that Milky Way globular clusters can be resolved into individual stars, so that their ages, metallicities, and masses can be determined with much higher accuracy through colour-magnitude diagram (CMD) isochrone fitting, and high-resolution spectroscopy.

Previous measurements of the total magnitudes of Galactic globular clusters were either based on aperture photometry (e.g. Hanes & Brodie 1985; Peterson 1986; Vanderbeke et al. 2014) or were derived by integrating the surface brightness profile of a cluster (e.g. McLaughlin & van der Marel 2005). Both approaches have problems distinguishing between field and cluster stars. In

addition, bright cluster giants are often excluded from the surface density profile, leading to a possible underestimation of the derived total cluster luminosity. These problems become more severe for bulge clusters that are located in regions of very high background stellar density and fainter clusters that contain only few giant stars.

Recent years have seen a rise in the publication of photometric catalogues presenting deep, *Hubble Space Telescope* (*HST*)-based photometry of the centres of globular clusters (e.g. Piotto et al. 2002; Sarajedini et al. 2007), as well as wide area, ground-based studies (e.g. Stetson et al. 2019). In addition, deep photometric data are nowadays also available from ground-based surveys like SDSS (Abazajian et al. 2003), 2MASS (Skrutskie et al. 2006), and DES (The Dark Energy Survey Collaboration 2005) or PanStarrs (Chambers et al. 2016). This makes it possible to determine the cluster magnitudes by summing up the magnitudes of the individual member stars. This allows to use the location of stars in a colour-magnitude diagram, as well as their proper motions from *Gaia* DR2 and their radial velocities (Baumgardt & Hilker 2018) to distinguish between cluster and field stars. In addition, *Gaia* proper motions and photometry can also be used to better determine the density profiles of clusters (De Boer et al. 2019). Both effects can be used to determine the total cluster magnitude with higher accuracy.

In the present paper, we use published photometry to determine new magnitudes and mass-to-light ratios of 153 Galactic globular clusters. We concentrate on the determination of *V*-band magnitudes since *V*-band data are available for the largest number of clusters. Our procedure can, however, easily be adopted to other wavelength bands. Our paper is organised as follows: In Section 2, we describe the input photometry used and explain our

Author for correspondence: H. Baumgardt, E-mail: h.baumgardt@uq.edu.au

Cite this article: Baumgardt H, Sollima A and Hilker M. (2020) Absolute *V*-band magnitudes and mass-to-light ratios of Galactic globular clusters. *Publications of the Astronomical Society of Australia* 37, e046, 1–18. <https://doi.org/10.1017/pasa.2020.38>

procedure to derive the total magnitudes. In Section 3, we compare our magnitudes with published literature values and calculate total magnitudes and mass-to-light ratios for all clusters. We draw our conclusions in Section 4.

2. Observational data

2.1. Input photometry

The photometry for the inner parts of globular clusters is mainly based on *HST*-based observations, since only *HST* has a sufficiently high spatial resolution to resolve the centres of dense globular clusters. Our main source for *HST*-based photometry is the ACS Survey of Galactic Globular Clusters (Sarajedini et al. 2007). The ACS Survey has observed the centres of 65 globular clusters using the F606W and F814W filters of the *HST* ACS/WFC camera. To this set of 65 clusters we add 14 clusters that have been observed mostly with the *HST* WFC3 camera in the F438W/F555W filters and were analysed by Baumgardt et al. (2019). We furthermore use F439W/F555W WFPC2 photometry from the HST Globular Cluster Snapshot Program (Piotto et al. 2002) for 19 globular clusters as well as a number of published literature observations for other clusters. Finally, for six globular clusters (AM 4, FSR 1735, NGC 6440, Pal 13, Sagittarius II, and Ter 3), we downloaded *HST* images from the STScI archive and performed stellar photometry using DOLPHOT (Dolphin 2000; 2016) on it. Photometry was performed on the CTE-corrected flc images, using the point-spread functions provided for each camera and filter combination by DOLPHOT. Where necessary, we first transformed the *HST* instrumental coordinates into equatorial coordinates by cross-matching stellar positions and magnitudes from *HST* with the positions of stars in the *Gaia* catalogue. In total, we have been able to obtain deep *HST* photometry, reaching between two to five magnitudes below the main-sequence turn-off for 126 globular clusters. The sources of the used *HST* photometry are listed in Table A.1. The remaining clusters are mostly low-mass and low-density clusters for which ground-based photometry should also be sufficiently complete for upper main sequence and giant stars.

Due to the small field of view, available *HST* photometry is largely limited to the innermost 120'' around the centres of globular clusters. For many globular clusters, this is less than the observed half-light radius. We therefore combine the *HST* photometry in the inner parts with ground-based photometry for the outer cluster parts. Our main source for ground-based photometry is the recent catalogue of ground-based photometry by Stetson et al. (2019). They present wide-field, ground-based photometry in the Johnson–Cousins UBVRI bands based on about 90 000 public and proprietary images for 48 Galactic globular clusters. We furthermore use unpublished data that were compiled in a similar way by Peter Stetson and that we downloaded from the Canadian Astronomy Data Centre^a for an additional 63 clusters. For globular clusters for which *V*-band data by P. Stetson are not available, we used other ground-based *V*-band data from the literature as indicated in Table A.1. Where necessary, we cross-correlated the ground-based data against the *Gaia* catalogue to convert instrumental (x/y) coordinates into (RA/Dec) coordinates.

^aThis data is available under <https://www.cadc-ccda.hia-ihp.nrc-cnrc.gc.ca/en/community/STETSON/index.html>.

For two clusters, ESO452-SC11 and IC1257, we performed our own photometry. We downloaded and reduced publicly available data in the *V* and *I* bands that were taken with EFOOSC (mounted on the NTT at La Silla) in May 2012 for ESO 452-SC11 [ESO programme ID: 089.D-0194(A)] and May 2015 for IC 1257 [ESO programme ID: 095.D-0037(A)]. We used DAOPHOT to perform PSF photometry on short and long exposures. The photometric calibrations based on colour terms and extinction coefficients provided by ESO for EFOOSC, and the zeropoints were adopted such that they match previous, shallower photometry in the Johnson–Cousins system by Cornish et al. (2006) for ESO452-SC11 and Harris et al. (1997) for IC1257.

We finally used data from the DECam Plane Survey (Schlafly et al. 2018) for clusters for which we could not find any other photometry. In total, we have been able to obtain deep ground-based photometry that covers the giant-branch and turnover regions for 136 globular clusters. The sources of the ground-based photometry for the individual clusters are listed in Table A.1.

2.2. Creation of a master catalogue

Since the *HST* photometry is not in the standard Johnson–Cousins UBVRI system, we first converted the magnitudes of the various *HST* camera systems into the Johnson UBVRI system. For *HST* photometry taken from Sarajedini et al. (2007) and Piotto et al. (2002), we use the BVI band magnitudes that were calculated by these authors. For the other data, we apply a magnitude transformation following Holtzman et al. (1995):

$$TMAG - SMAG = c_0 + c_1 \times TCOL + c_2 \times TCOL^2, \quad (1)$$

where TMAG is a magnitude in the target system, SMAG is a magnitude in the source system, c_0 , c_1 , and c_2 are transformation constants, and TCOL is the difference between two magnitudes in the target system. Since the right-hand side requires a magnitude difference in the target system, we apply the above transformations iteratively, using the colour difference in the source system as starting value. In order to convert *HST*/WFPC2 magnitudes to UBVRI magnitudes, we use the coefficients given in Table 7 of Holtzman et al. (1995). For the transformation of *HST*/ACS magnitudes, we use the transformation coefficients given in Table 18 of Sirianni et al. (2005), while the conversion of *HST* WFC3/UVIS magnitudes is done using the coefficients given in Table 2 of Harris (2018).

To increase the accuracy of the transformed BVI magnitudes that we obtain from the *HST* photometry, we compare them against ground-based BVI magnitudes for the stars in common. For the clusters listed in Table 2 that have ground-based photometry, we use the same ground-based photometry for calibration that we also use for the outer cluster parts. For three of the remaining clusters without ground-based photometry (NGC 6293, NGC 6304, NGC 6540), we use the photometry from Peter Stetson's standard star archive (Stetson 2000). The resulting magnitude shifts are mostly below 0.05 mag, except for a few heavily reddened bulge clusters for which the corrections can reach 0.2 mag.

After transforming the *HST* magnitudes to the Johnson–Cousins system, we create a master catalogue for each cluster by combining the *HST* photometry in the inner parts with the ground-based photometry in the outer cluster parts. We cross-match the positions of stars in the *HST* catalogue with those from the ground-based photometry using a search radius of 0.5 arcsec. Since the *HST* photometry has a higher precision than the

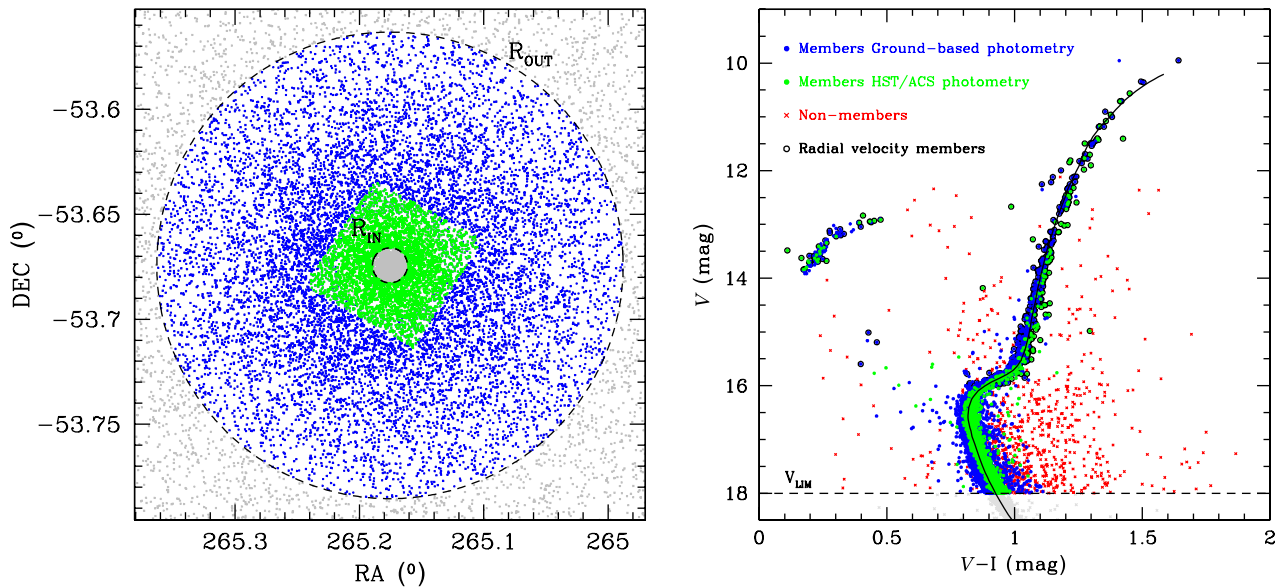


Figure 1. Illustration of our member star selection approach for the globular cluster NGC 6397. The left panel shows an $800'' \times 800''$ arcsec field centred on the cluster. Stars selected from *HST/ACS* observations are shown in green, stars from the ground-based photometry of Stetson et al. (2019) in blue. The dashed circles show the limits of the field for which we determine the cluster luminosity. The right panel shows a CMD of NGC 6397 with a 12 Gyr old PARSEC isochrone overlaid as solid line. Blue and green circles depict cluster members, while red crosses depict stars classified as non-members based on their CMD position, *Gaia* proper motion, or radial velocity. The dashed line marks the lower limit down to which we use observed stars. Circles mark radial velocity members.

ground-based photometry in the crowded cluster centres, we keep the *HST* photometry for the stars that are in common between both data sets. Figure 1 illustrates our member search approach for the cluster NGC 6397.

2.3. Selection of cluster members

Cluster members are selected from the photometric master catalogue based on three criteria: Position in the CMD, radial velocity, and *Gaia* proper motion. In order to select stars based on photometry, we fit PARSEC isochrones (Bressan et al. 2012) to each cluster and use these to select main sequence and giant star members. Possible cluster members must either have a colour difference no larger than 2.5 times their photometric error from the best-fitting isochrone or have a colour difference less than a maximum value. We choose the maximum colour difference individually for each cluster based on the observed width of the RGB and the amount of background contamination. For most clusters, these values are usually around 0.20 mag. We also select stars as potential cluster members if they are located in the CMD in the region that correspond to horizontal-branch stars and blue stragglers. For a few clusters with strong and variable reddening, we first derive a de-reddened CMD by shifting stars along the reddening vector to a common main sequence and then identify cluster members in the de-reddened CMD.

Our second criterion for membership determination is the stellar radial velocities compiled by Baumgardt (2017) and Baumgardt & Hilker (2018). Their data contain radial velocities and membership information for about 250 000 stars in the fields of globular clusters. We cross-match the positions of all stars that are classified as members based on CMD position with the radial velocities of Baumgardt & Hilker (2018) and keep only those stars that either have no radial velocity measurement or have a radial velocity that

is within $\pm 2.5\sigma$ of the cluster mean velocity. Here the velocity dispersion σ is calculated at the position of each star based on the best-fitting N -body model of Baumgardt & Hilker (2018).

We finally use the *Gaia* DR2 proper motions and parallaxes for membership determination. For stars that have passed the CMD and radial velocity tests, we cross-match their positions against the positions of stars in the *Gaia* catalogue and require that their proper motion is within 2.5σ of the mean cluster proper motion determined by Baumgardt et al. (2019). We also require that the star has a parallax that is compatible with the cluster parallax $p_{CL} = 1/d$ where d is the cluster distance given by Baumgardt & Hilker (2018). We keep all stars that have no *Gaia* counterparts. Stars without *Gaia* counterparts are either faint stars or stars in the centres of clusters that have a high chance of being cluster members due to the strong density contrast between cluster and field stars in the centre.

2.4. Magnitude determination

We calculate the total luminosity of the cluster members determined in the previous section according to:

$$L_{V_{Obs}} = \sum_i 10^{-0.4V_i} \quad (2)$$

To derive the total cluster luminosities from $L_{V_{Obs}}$, we then need to correct $L_{V_{Obs}}$ for faint stars not included in the photometry, cluster regions that are not covered by the photometry, and any background contamination remaining in the data.

We correct for incompleteness at the faint end by imposing a magnitude cut-off V_{LIM} that is bright enough that the photometry is still complete for stars brighter than V_{LIM} but faint enough that stars fainter than V_{LIM} contribute only a small fraction of the cluster light. We usually choose V_{LIM} to be one or two magnitudes below the main-sequence turn over, depending on the quality of the photometry and the distance of the cluster. This

guarantees that the directly measured bright stars already contribute between 80 and 90% of the total cluster luminosity. We estimate the contribution of the fainter stars based on the N -body models of Baumgardt & Hilker (2018). Baumgardt & Hilker (2018) ran a grid of about 3 000 N -body simulations and determined for each cluster the N -body model that produced the best fit to the observed stellar mass function at different radii, the observed surface density profile, and the observed velocity dispersion profile. Their simulations provide for each globular cluster a star-by-star model containing main-sequence, giant stars, and compact remnants. For each star, we use the bolometric luminosity, surface temperature, and metallicity from the N -body model and convert these into UBVRI magnitudes using the Kurucz (1992) atmosphere models for nuclear burning stars and the bolometric corrections and colour indices calculated by Bergeron et al. (1995) for white dwarfs. After the conversion, we calculate the total V band luminosity, of all stars $L_{\text{Sim},A}$ and the one for only the bright stars $L_{\text{Sim},B}$ with $V < V_{\text{Lim}}$, and correct the observed cluster luminosity by $L_{V,\text{In}} = L_{V,\text{Obs}} \cdot L_{\text{Sim},A} / L_{\text{Sim},B}$. Varying V_{Lim} for a few nearby clusters with deep photometry shows that the derived luminosities vary by only about ± 0.03 mag when decreasing the magnitude limit V_{Lim} .

In order to estimate the contribution of the cluster parts that are either excluded due to crowding or not covered by the photometry to the total cluster luminosity, we again use the best-fitting N -body model of each cluster and calculate the total cluster luminosity $L_{\text{Sim},T}$ and the luminosity of the part that is covered by the photometry $L_{\text{Sim},\text{In}}$. We then calculate the total cluster luminosity by $L_{V,\text{Tot}} = L_{V,\text{In}} \cdot L_{\text{Sim},T} / L_{\text{Sim},\text{In}}$. Once the total cluster luminosity has been calculated, we calculate the total magnitude of the cluster as $V = -2.5 \cdot \log_{10} L_{V,\text{Tot}}$. For a few bulge clusters, background contamination is an issue even after selecting stars based on CMD position, radial velocities, and *Gaia* proper motions and parallaxes. In order to correct the cluster luminosity for background stars, we integrate the cluster profile out to large radii so that we can determine the surface brightness of background stars and then subtract the total luminosity of the background stars from the cluster luminosity. Table B.1 presents the total cluster luminosities that we derive this way. It also presents the absolute magnitudes that we calculate from the apparent magnitudes using the extinction values from Harris (1996) as well as the cluster distances from Baumgardt et al. (2019) and the radii containing 10% and 50% of the cluster light in projection together with the surface brightness at these radii.

We estimate the error of the cluster luminosity as follows: For clusters where we have no photometry in the Johnson–Cousins system with which to correct the *HST* magnitudes, we assume an error of $\Delta V = 0.10$ mag on the total cluster luminosity. We assume that this error drops to $\Delta V = 0.04$ mag for clusters where we have ground-based V band magnitude measurements. The latter value is equal to the maximum zero-point uncertainty estimated by Stetson et al. (2019) for their photometry. We also assume that the correction factors $f_{\text{Bright}} = L_{\text{Sim},A} / L_{\text{Sim},B} - 1$ and $f_{\text{Field}} = L_{\text{Sim},T} / L_{\text{Sim},\text{In}} - 1$ have 10% relative errors, i.e. if $f_{\text{Bright}} = 0.20$, we assume that the corresponding correction of the cluster luminosity has a relative error of 2%, leading to a 0.022 mag uncertainty of the total cluster magnitude. We also assume that the global mass function slopes α determined by Baumgardt & Hilker (2018) have uncertainties of ± 0.20 . Experiments show that the final cluster luminosity changes by 0.02 mag for a change

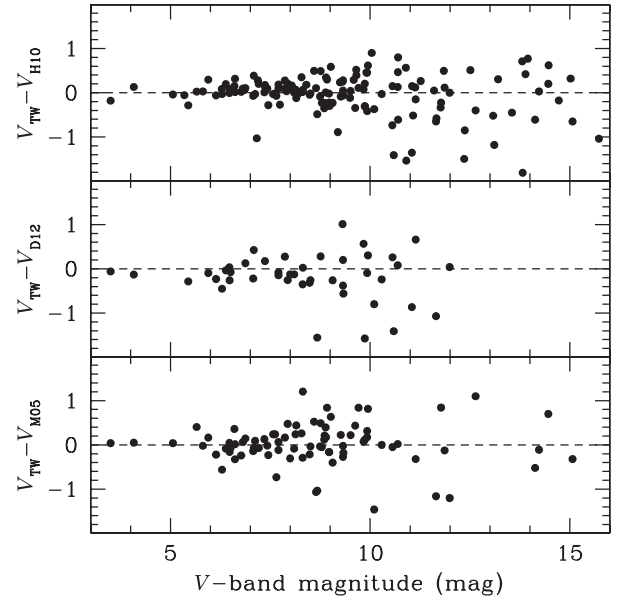


Figure 2. Difference in the total magnitudes between this work and (from top to bottom) the 2010 version of Harris (1996) (H10), Dalessandro et al. (2012) (D12), and McLaughlin & van der Marel (2005) (M05). The differences increase for fainter clusters and can reach up to two magnitudes for individual clusters.

of α of 0.20. Finally, for those clusters where we subtracted a background contribution, we vary the assumed background level by 10% and assume an additional magnitude error equal to the change in total cluster magnitude caused by this variation of the assumed background level. The total magnitude error is then calculated combining the various magnitude uncertainties, which we assume to be statistically independent. The magnitude errors are also given in Table B.1. For the best observed clusters, we can achieve errors better than 0.05 mag, i.e. luminosities accurate to about 5%.

3. Results

3.1. Apparent magnitudes

Figure 2 and Table 1 compare the apparent magnitudes derived here with those given in the 2010 version of Harris (1996), (H10) Dalessandro et al. (2012) (D12), and McLaughlin & van der Marel (2005) (M05). The magnitudes from Harris (1996) are mainly derived from aperture photometry, while McLaughlin & van der Marel (2005) derived magnitudes through an integration of the surface density profiles of Trager et al. (1995). Dalessandro et al. (2012) derived total magnitudes from data of the *GALEX* satellite. Hence, all estimates use different input data and are more or less independent of each other. We therefore average the literature estimates and compare them with the magnitudes derived here in the last row of Table 1. Only clusters that have at least two magnitude determinations in the literature are used in the last row.

The literature values show good agreement with our measurements only for bright clusters with $V < 8$ mag, where the average difference is close to zero and the typical deviation for individual clusters is about 0.20 mag. For clusters with total magnitudes fainter than 8 mag, the differences quickly increase and can be as large as 2 mag for some clusters fainter than $V = 11$ mag.

Table 1. Mean differences and standard deviation around the mean between our photometry and literature values for three different magnitude ranges.

Paper	$V < 8$		$8 < V < 11$		$V > 11$	
	$\langle \Delta V \rangle$ (mag)	σ_V (mag)	$\langle \Delta V \rangle$ (mag)	σ_V (mag)	$\langle \Delta V \rangle$ (mag)	σ_V (mag)
Harris (2010)	+0.03	0.22	+0.01	0.45	-0.25	0.70
Dalessandro et al.	-0.07	0.21	-0.25	0.66	-0.31	0.81
McLaughlin & vdM	-0.02	0.25	+0.08	0.51	-0.10	0.80
Literature averaged	+0.01	0.15	+0.03	0.35	-0.03	0.53

For all magnitude ranges, the differences are much larger than what we expect based on our magnitude errors, indicating that the differences are mainly due to inaccuracies in the literature magnitudes. Interestingly, averaging the literature magnitudes already leads to significantly smaller scatter than derived from the individual data sets. A closer examination shows that the most discrepant clusters are often relatively low-mass clusters like Pal 11 ($M = 1.0 \cdot 10^4 M_\odot$), Ter 8 ($M = 5.9 \cdot 10^4 M_\odot$), or Arp 2 ($M = 3.9 \cdot 10^4 M_\odot$). Since most of these clusters are located in areas of low field-star contamination, have both deep and ground-based photometry, and have proper motions that clearly separate the cluster from the field stars, we regard our total magnitudes as very reliable. The reason for the strong discrepancy with the literature values could be that the aperture photometry measurements and the surface brightness profiles of Trager et al. (1995) have excluded bright giant stars in order to obtain smooth density profiles. This could explain why for the faintest clusters our magnitude values are on average smaller (meaning we derive larger total luminosities) compared to the literature values. It could also explain why more massive and brighter clusters show better agreement, since the effect of single bright stars is smaller in more massive clusters. The remaining clusters that show large differences are mostly bulge clusters like NGC 6256, NGC 6453, or NGC 6749 which are located in fields with a large background density of stars. Since we use *Gaia* proper motions to clean the CMDs from field stars, we again expect our magnitudes to be more reliable than the literature ones.

3.2. Absolute cluster magnitudes

In order to convert the apparent magnitudes to absolute ones, we use the cluster distances from Baumgardt et al. (2019) and the $E(B - V)$ values given by Harris (1996). Figure 3 depicts the distribution of absolute magnitudes of globular clusters that we derive this way, split up into the full sample (upper panel), inner clusters with galactocentric distances $R_{GC} < 15$ kpc (middle panel), and outer clusters with $R_{GC} > 15$ kpc (lower panel). Fitting a Gaussian to the distribution, we obtain a mean magnitude of $M_V = -7.13$ and a width of $\sigma_V = 1.47$ for the full cluster sample. Our mean absolute magnitude is about 0.2–0.3 mag lower, and the width is significantly higher than what has been found previously (e.g. Secker 1992; Di Criscienzo et al. 2006). The main reason for the difference is the many low-mass clusters that have been discovered in recent years: For example, out of the 15 globular clusters known today that are not included in the sample of Di Criscienzo et al. (2006), 14 have absolute luminosities below the mean. It is therefore likely that the average luminosity of MW globular clusters

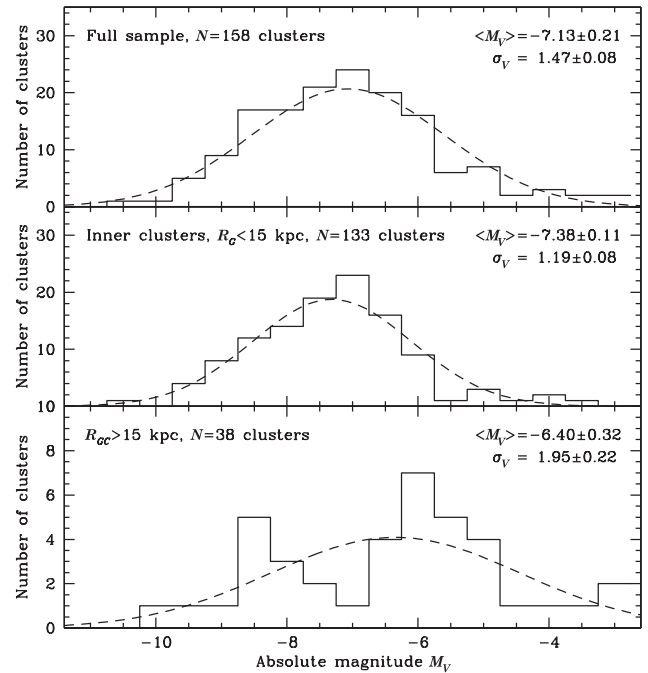


Figure 3. Distribution of absolute magnitudes of Milky Way globular clusters. The top panel shows the full distribution, the middle panel the distribution of inner clusters with $R_G < 15$ kpc, and the lower panel the distribution of outer clusters with $R_G > 15$ kpc. The distribution of outer clusters contains a significantly larger fraction of low-luminosity clusters.

could be lower since our census of globular clusters in the inner parts of the Milky Way is probably still not complete (Minniti et al. 2017). The middle and lower panels of Figure 3 split the cluster sample into an inner sample inside $R_{GC} = 15$ kpc and an outer one. For the inner clusters, we obtain a mean of $M_V = -7.39$ with a width of $\sigma_V = 1.19$. Both values do not seem to depend on the radial range that we consider, indicating that the globular cluster luminosity function is invariant in the inner parts of the Milky Way. In contrast, the outer clusters have a significantly lower mean luminosity of $M_V = -6.40$ and a much larger width. Huxor et al. (2014) found evidence that the outer globular cluster system of the Andromeda Galaxy has a bi-model distribution in luminosity, with a second peak at $M_V = -5.5$. The Milky Way globular cluster system could show a similar bi-modality, with one peak at around $M_V = -8$, similar to the inner globular clusters, and a second peak around $M_V = -6$. Huxor et al. (2014) also speculated that the bright outer-halo clusters in M31 formed in situ, while the clusters in the fainter peak are accreted from dwarf galaxies. Current orbital data on the Milky Way globular clusters, however, do not support this conclusion: Out of the 14 globular clusters that are at distances $R_G > 15$ kpc and that are brighter than $M_V = -7.0$, all are associated with a dwarf galaxy progenitor (Gaia-Enceladus, Sagittarius or Helmi Streams) in the recent study by Massari et al. (2019). In contrast, among the 23 outer clusters fainter than $M_V = -7.0$, only 9 are considered securely and 3 are possibly associated with a dwarf galaxy progenitor according to Massari et al. (2019). Hence, many of the faint globular clusters could have formed in situ in the halo of the Milky Way without a connection to a dwarf galaxy. Alternatively, they could be associated with dwarf galaxies that have not yet been discovered.

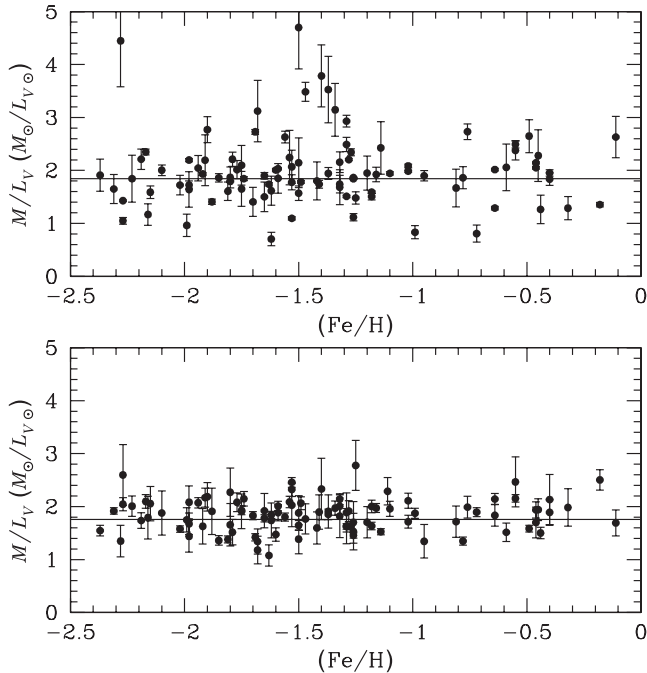


Figure 4. M/L_V mass-to-light ratios derived using masses and distances from Baumgardt et al. (2019), extinction values from Harris (1996), and literature averaged V -band luminosities (top panel). The bottom panel shows the mass-to-light ratios derived with the same data but our V band magnitudes. The resulting M/L_V ratios cover a much smaller scatter around the mean value (marked by a solid line).

3.3. Cluster M/L_V ratios

Figure 4 compares the mass-to-light ratios that we derive from our magnitudes with the M/L_V ratios that we derive from the literature averaged V -band luminosities. In order to calculate the cluster mass-to-light ratios, we use the cluster masses and distances from Baumgardt et al. (2019) and the extinction values given by Harris (1996). We only plot clusters that have relative mass uncertainties $\Delta M/M < 0.2$ in Figure 4 in order to be able to better judge the quality of the cluster luminosities. For the same reason, we restrict ourselves to clusters with extinction values $E(B - V) < 1.0$ since for highly reddened clusters differential extinction or uncertainties in the reddening could introduce additional uncertainties. We obtain an average mass-to-light ratio of $M/L_V = 1.83 \pm 0.03 M_\odot/L_\odot$ and a standard deviation of $\sigma_{M/L} = 0.24 \pm 0.03 M_\odot/L_\odot$ around the mean using our magnitudes compared to $M/L_V = 1.92 \pm 0.05 M_\odot/L_\odot$ and $\sigma_{M/L} = 0.49 \pm 0.05 M_\odot/L_\odot$ that we derive from the literature magnitudes. Hence, while the average mass-to-light ratio changes by only $0.1 M_\odot/L_\odot$, we obtain a much more uniform M/L_V distribution using our magnitudes. In particular, using our magnitudes, no clusters have mass-to-light ratios $M/L_V > 2.5 M_\odot/L_\odot$ or $M/L_V < 1 M_\odot/L_\odot$, which would be hard to explain using standard isochrones (see Section 3.2).

The M/L ratio of a cluster is influenced by several different processes: First, stellar evolution leads to an increase of the M/L ratio with time as massive and bright stars, which are contributing to the total cluster light more than to the cluster mass, are constantly being turned into compact remnants. According to the PARSEC isochrones (Bressan et al. 2012), stellar evolution should increase the M/L_V ratio of a globular cluster by about $0.3 M_\odot/L_\odot$ when the cluster age increases from $T = 10$ Gyr to $T = 13.5$ Gyr, with only a weak dependence of this increase on metallicity. Second, the

stellar mass function of a cluster changes as a result of mass segregation, which lets massive stars sink into the centre and moves low-mass stars towards the outer cluster parts where they are preferentially removed due to an external tidal field. Baumgardt & Makino (2003) found by means of N -body simulations that this process leads initially to a decrease of the cluster M/L ratio since low-mass stars mainly contribute to the cluster mass and only little to the overall cluster light, followed by an increase very close to final dissolution when mainly compact remnants are left in the cluster. Baumgardt & Makino (2003) found a maximum decrease of the M/L ratio of about $\Delta M/L_V = 0.5$ to 0.7 due to mass loss. A decrease of the cluster M/L ratio during the evolution was also found by Bianchini et al. (2017), although they found that the ejection of dark remnants is also important in changing the M/L ratio of a star cluster. Finally, M/L ratios also depend on the metallicity of a cluster. Maraston (1999) predicted an increase of the V -band M/L ratio by a factor three when increasing the metallicity from $[\text{Fe}/\text{H}] = -0.5$ to $[\text{Fe}/\text{H}] = +0.3$.

Figures 5 and 6 depict the dependence of the M/L ratios that we derive from our magnitudes on the cluster age and mass function slope α . Similar to the previous plots, we show only clusters that have relative mass errors $\Delta M/M < 0.2$ and reddening values $E(B - V) < 1.0$. We also divide the sample into low-metallicity clusters with $[\text{Fe}/\text{H}] < -1.5$ and high-metallicity clusters with $[\text{Fe}/\text{H}] > -1.5$ to reduce the dependency on metallicity. We have taken the cluster ages in Figure 5 mainly from VandenBerg et al. (2013), or, if a cluster was not studied by them, from the literature. We obtain highly significant positive Spearman rank-order coefficients r_s for both metallicity ranges. Also a linear fit of the form $M/L_V = x + y \cdot T_{\text{Age}}$ gives positive slopes y for both metallicity ranges, indicating that cluster M/L ratios increase with age. The increase seen when going from $T = 10$ Gyr to $T = 13.5$ Gyr is about $0.45 M_\odot/L_\odot$ for both metal-poor and metal-rich clusters, in agreement with the predicted change based on stellar isochrones.

Figure 6 depicts the M/L_V ratios against the mass function of the clusters, taken from Baumgardt et al. (2019). We obtain a weak anti-correlation between the mass-to-light ratio of a cluster and its mass function slope α only for the metal-poor clusters. For the metal-rich clusters, there is no visible correlation. One reason for the lack of a correlation for metal-rich clusters could be that either the mass or mass function measurements for these have large errors since many of these clusters are located in the bulge, which makes observations of them more difficult. Alternatively, clusters could start with different initial mass functions, so the present-day differences in the MF slope α are not due to dynamical evolution.

3.4. Contribution of different stars to the total magnitudes

Table 2 shows the contribution of stars in different evolutionary stages to the total V -band magnitudes. We have split stars into main sequence stars (MS), horizontal branch stars (HB), blue stragglers (BS), and red giant branch stars (RGB), where the RGB stars include asymptotic giant branch and sub-giant branch stars as well. As an example, Figure 7 depicts the division of stars for two clusters, NGC 6528 and NGC 7078. We have analysed six clusters, roughly equally spaced in metallicity between $[\text{Fe}/\text{H}] = -2.37$ to $[\text{Fe}/\text{H}] = -0.11$, thereby encompassing the range of metallicities seen for Galactic globular clusters. We again use our N -body models to correct for main-sequence stars too faint to be seen in the observations.

Table 2. Relative contribution of stars in different evolutionary stages to the total V-band magnitudes for six clusters.

Cluster	[Fe/H]	BS (%)	HB (%)	RGB (%)	MS (%)
NGC 6528	-0.11	1.3	22.4	51.1	25.0
NGC 6496	-0.46	0.8	12.2	59.8	27.2
NGC 6171	-1.02	0.9	13.8	57.1	28.3
NGC 5272	-1.50	0.3	10.9	55.9	32.9
NGC 6397	-2.02	0.3	9.5	60.8	29.3
NGC 7078	-2.37	0.2	8.9	52.4	38.6

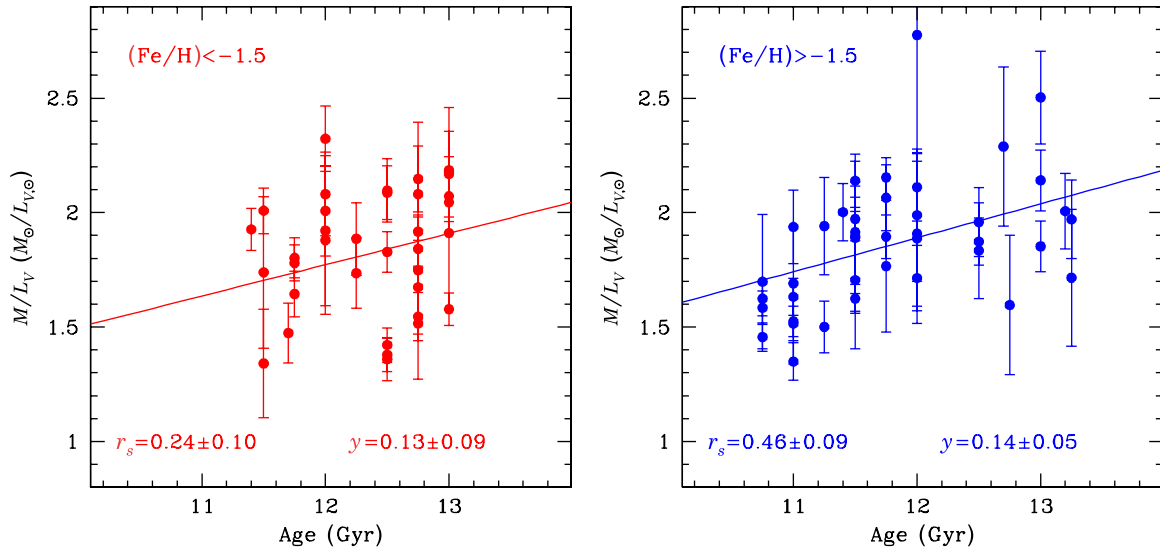


Figure 5. Dependence of mass-to-light ratio on the cluster ages for two different metallicity ranges. The M/L ratio increases as a function of age in agreement with theoretical predictions. The plots also show the Spearman rank-order coefficient r_s as well as the slope y of the best-fitting linear fit to the data.

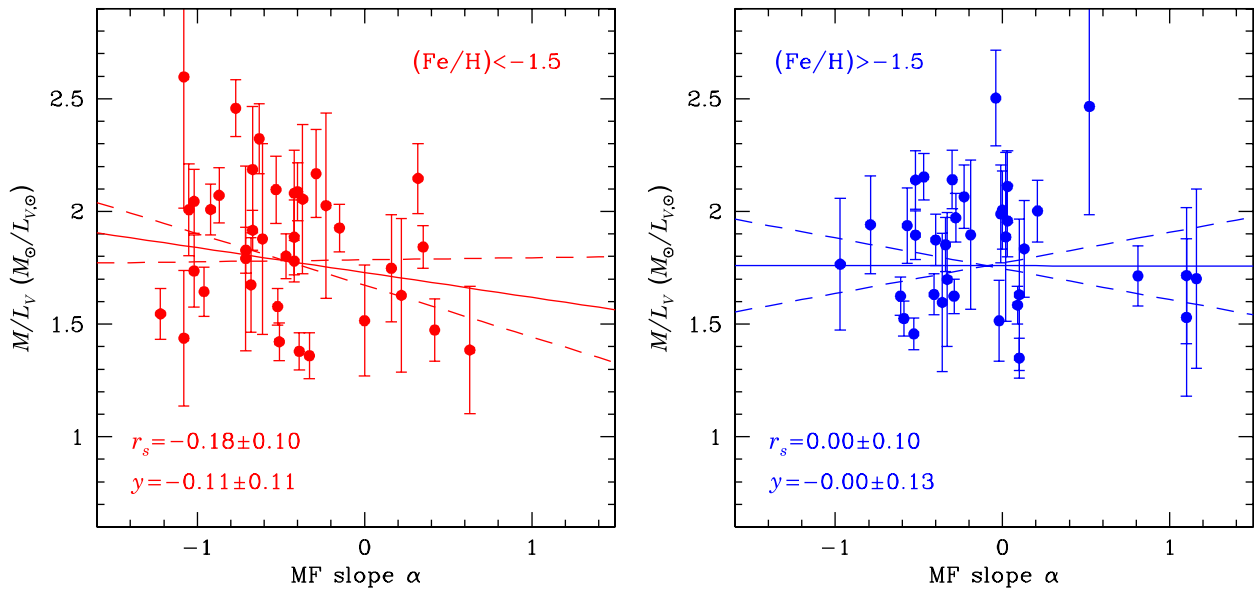


Figure 6. Same as Figure 5 but this time showing the dependence of mass-to-light ratio on the mass function of clusters.

It can be seen that blue stragglers contribute only about $\sim 1\%$ to the total cluster light, with a strong increase of their contribution towards higher metallicity. The fraction of light from HB stars is also increasing with metallicity, while the fraction of light coming

from the RGB is roughly constant at around 55%. The increase of the fraction of light in HB stars at increasing metallicity confirms predictions by stellar evolution models (e.g. Renzini & Buzzoni 1986), which predict such an increase as a result of the shorter

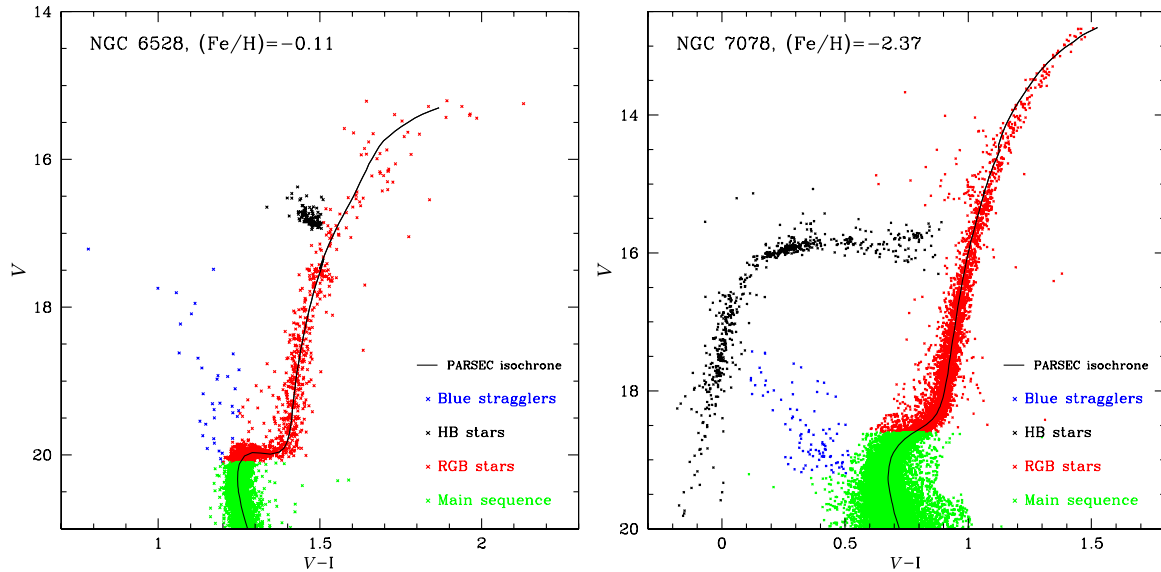


Figure 7. Illustration of our division of stars into different evolutionary stages for the high metallicity cluster NGC 6528 (left panel) and the low metallicity cluster NGC 7078 (right panel). Stars are split into blue stragglers (blue), horizontal branch stars (HB, black), red giant branch stars (RGB, red), and main sequence stars (green). Only stars that pass the various membership criteria detailed in Section 2 are shown.

evolutionary timescales on the RGB stars. There also seems to be a slight decrease of the fraction of light from MS stars with metallicity; however, this decrease could also be driven by other factors like a change of the internal mass function of the clusters. A larger sample would be needed to disentangle the different effects.

3.5. Comparison with stellar evolution models

Figure 8 depicts the ratio of the M/L_V values that we derive from our apparent cluster magnitudes with the predictions of stellar evolution models. Shown are predictions from version 1.2 of the MIST isochrones (Paxton et al. 2015; Dotter 2016; Choi et al. 2016), version 1.2 of the PARSEC isochrones (Bressan et al. 2012), and predictions from the DARTMOUTH isochrones (Dotter et al. 2008a). For each stellar evolution model, we created a two-dimensional grid of isochrones in age and metallicity. Isochrones were spaced by 0.5 Gyr between 10 Gyr and 13.5 Gyr in age and by $\Delta [Fe/H] = 0.10$ between $[Fe/H] = -2.50$ and $[Fe/H] = 0.0$ in metallicity. For each cluster age, metallicity, and stellar evolution model, we then distributed $5 \cdot 10^5$ stars following the mass functions given in Baumgardt & Hilker (2018) and then used the isochrones to calculate the total luminosity, total mass, and M/L ratio of each model. We thus obtained a grid of 1 456 models giving the M/L_V ratio of star clusters as a function of cluster age, metallicity, and internal mass function for each stellar evolution model. We then linearly interpolate in this grid of models to predict the expected mass-to-light ratio of each globular cluster given its mass function, metallicity, and cluster age.

Figure 8 compares the ratio of the observed M/L_V ratios to the theoretically predicted ones. It can be seen that the predictions of the MIST and PARSEC isochrones are very similar. Both reproduce the observed mass-to-light ratios of metal-rich clusters quite well, but predict higher than observed M/L_V ratios for the metal-poor clusters. The mismatch between observed and predicted M/L_V ratios of metal-rich globular clusters noted by Strader et al. (2011) is therefore mainly due to the fact that Strader

et al. (2011) assumed a Kroupa or Salpeter type mass function for the clusters, while the data for the Milky Way globular clusters indicate that they follow much shallower mass functions. At the moment, the data do not support a metallicity-dependent top-heavy IMF as suggested by Zonoozi et al. (2016), although we cannot rule out any such variation either.

A possible reason for the mismatch between predicted and observed M/L_V ratios of metal-poor globular clusters could be that the isochrone models considered a solar-abundance pattern, while metal-poor stars are known to be enriched in α -elements (Pritzl et al. 2005). The lower-left hand figure therefore compares our observed M/L_V ratios with DARTMOUTH isochrones that have an α -element enhancement of $[\alpha/Fe] = +0.2$. We use DARTMOUTH isochrones since for MIST and PARSEC isochrones only solar abundance models are available. It can be seen that for α -enhanced isochrones, the predicted M/L_V ratios of metal-poor clusters with $[Fe/H] < -1$ are in agreement with the observed ones, while the metal-rich clusters now have too low M/L_V ratios. However, there are indications that the α -element enhancement of globular clusters decreases for clusters with $[Fe/H] > -1$ down to solar values (e.g. Ferraro et al. 1999; Pritzl et al. 2005). Figure 3 in Horta et al. (2020), for example, shows that clusters with $[Fe/H] < -0.7$ have more or less constant $[Si/Fe]$ of about $[Si/Fe] = +0.25$, followed by a downturn in the $[Si/Fe]$ values similar to what is seen for field stars. The two most metal-rich clusters in their sample (Liller 1 and Pal 10) have $[Si/Fe]$ of 0.01 ± 0.05 and 0.0 ± 0.10 , respectively, i.e., they are compatible with a solar abundance ratio. A downturn of the α -element abundances for metal-rich globular clusters is also predicted based on cosmological simulations (e.g. Hughes et al. 2020).

We therefore adopt an α -element distribution with $[\alpha/Fe] = +0.2$ for clusters with $[Fe/H] < -0.8$ followed by a linear decrease down to $[\alpha/Fe] = +0.0$ for $[Fe/H] = 0.0$ and interpolate in our grid between the $[\alpha/Fe] = +0.2$ DARTMOUTH models and the PARSEC models depending on the α -element enhancement of each cluster. The resulting M/L_V ratios are shown in the lower

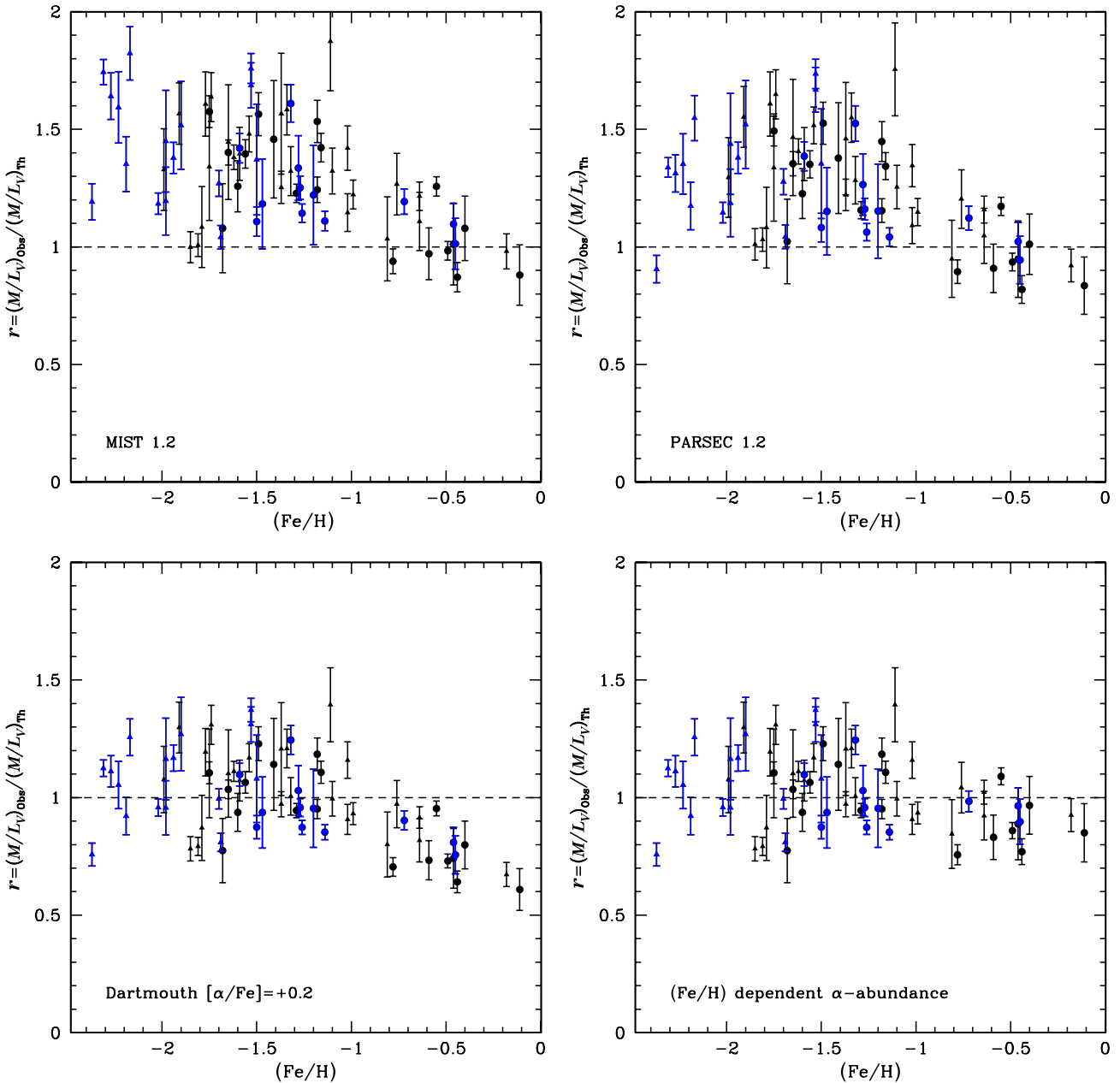


Figure 8. Ratio of the measured M/L_V ratios to the M/L_V ratio predicted by different stellar-evolution models as a function of the cluster metallicity. Shown is a comparison against MIST isochrones (top left), PARSEC isochrones (top right), Dartmouth isochrones with enhanced α element ratios of $[\alpha/Fe]=+0.2$ and a model in which the α -element abundances decrease for metal-rich clusters (lower right).

right corner. It can be seen that we now obtain an excellent agreement between the observed and expected mass-to-light ratios at all metallicities.

4. Conclusion

We have derived new V -band magnitudes of 153 Galactic globular clusters by summing up the magnitudes of their individual members stars derived from *HST* and ground-based photometry and correcting the derived magnitudes for missing faint stars and spatial incompleteness. In order to differentiate between cluster and field stars, we have made use of the positions of stars in

colour-magnitude diagrams, available radial-velocity information, and proper motions and parallaxes from *Gaia* DR2. Our V -band magnitudes show good agreement with published literature magnitudes for bright clusters with $V < 8$ mag. For fainter clusters, typical differences are of order 0.5 mag with individual clusters showing differences of up to 2 mag.

Our V -band magnitudes lead to a mean mass-to-light ratio of $M/L_V = 1.83$ and a scatter of $\sigma_V = 0.24 M_\odot/L_\odot$ around the mean, significantly smaller than the scatter obtained with literature magnitudes. In agreement with Strader et al. (2011), we find no dependence of the average mass-to-light ratio of a cluster with metallicity. We find evidence that the mass-to-light ratios of globular

clusters are increasing with cluster age, in agreement with theoretical predictions. We also find good agreement between the derived mass-to-light ratios with the expected ones from stellar isochrones if the mass function of the clusters is taken into account. PARSEC and MIST stellar isochrones with a solar-abundance pattern for α -elements are able to reproduce the mass-to-light ratios only for clusters with $[\text{Fe}/\text{H}] > -1.0$, but predict too high mass-to-light ratios for the more metal-poor clusters. However, using α -enhanced DARTMOUTH isochrones with $[\alpha/\text{Fe}] = +0.2$ leads to a good agreement of observed and predicted M/L ratios. There is, therefore, no evidence for a significant amount of dark matter inside the main body of globular clusters as has been previously suggested (Baumgardt & Mieske 2008; Wirth, Bekki, & Hayashi 2020). However, the data do not rule out dark matter haloes surrounding globular clusters or a small amount (of order 20% of the total mass or less) of dark matter inside the clusters.

We finally find that globular clusters at galactocentric distances $R_G > 15$ kpc have on average about one magnitude lower absolute magnitudes than clusters inside this radius. This could be either due to the weaker tidal field in the outer parts of the Milky Way, which increases the lifetime of low mass clusters to more than a Hubble time, or due to the fact that low-mass clusters in the inner Milky Way have not yet been found due to large reddening and the strong background density of stars. About half of the low-luminosity clusters in the outer parts are not connected to any known dwarf galaxy or any known past merger events that are thought to have happened in the early Milky Way, indicating that they either formed in situ or are connected to so far undiscovered dwarf galaxies.

In the future, determining total magnitudes, cluster colours, and M/L ratios in other wavelength bands will be useful for tests of stellar evolution and galactic studies. Given our photometric data and the fact that we already have determined the cluster members, this task should also be straightforward to implement. Our photometry should also help determine the contribution of stars in different evolutionary stages (RGB, HB, main sequence, and blue stragglers) to the total magnitudes in the different bands. The caveat, however, is that individual stellar photometry in bands other than the V band is currently only available for a subset of Galactic clusters.

Acknowledgements. The authors thank Sylvie Beaulieu, Aaron Dotter, Matthias Frank, Edoardo P. Lagioia, Domenico Nardiello, Stefano Oliveira de Souza, Soeren S. Larsen, Sebastian Kamann, Jeffrey Simpson, and Daniel Weisz for sharing their globular cluster photometry with us. The authors also acknowledge the work by Peter Stetson in deriving wide-field, ground-based photometry of globular clusters and making his data public before publication. The authors finally thank Mirek Giersz and Jarrod Hurley for making a FORTRAN code available to us that converts bolometric luminosities and temperatures into absolute magnitudes in the Johnson-Cousins system. Based on observations made with the NASA/ESA Hubble Space Telescope, obtained from the data archive at the Space Telescope Science Institute. STScI is operated by the Association of Universities for Research in Astronomy, Inc. under NASA contract NAS 5-26555. This research has made use of the SIMBAD database, operated at CDS, Strasbourg, France. This work has made use of data from the European Space Agency (ESA) mission *Gaia* (<https://www.cosmos.esa.int/gaia>), processed by the *Gaia* Data Processing and Analysis Consortium (DPAC, <https://www.cosmos.esa.int/web/gaia/dpac/consortium>). Funding for the DPAC has been provided by national institutions, in particular the institutions participating in the *Gaia* Multilateral Agreement.

References

- Abazajian, K., et al. 2003, *AJ*, **126**, 2081
 Alcaino, G., Liller, W., Alvarado, F., & Wenderoth, E. 1991, *AJ*, **102**, 1371
 Barbuy, B., Ortolani, S., & Bica, E. 1997, *A&AS*, **122**, 483
 Baumgardt, H. 2017, *MNRAS*, **464**, 2174
 Baumgardt, H., & Hilker, M. 2018, *MNRAS*, **478**, 1520
 Baumgardt, H., & Makino, J. 2003, *MNRAS*, **340**, 227
 Baumgardt, H., & Mieske, S. 2008, *MNRAS*, **391**, 942
 Baumgardt, H., Hilker, M., Sollima, A., & Bellini, A. 2019, *MNRAS*, **482**, 5138
 Beaulieu, S. F., Gilmore, G., Elson, R. A. W., Johnson, R. A., Santiago, B., Sigurdsson, S., & Tanvir, N. 2001, *AJ*, **121**, 2618
 Beccari, G., Bellazzini, M., Lardo, C., Bragaglia, A., Carretta, E., Dalessandro, E., Mucciarelli, A., & Pancino, E. 2013, *MNRAS*, **431**, 1995
 Bergeron, P., Wesemael, F., & Beauchamp, A. 1995, *PASP*, **107**, 1047
 Bianchini, P., Sills, A., van de Ven, G., & Sippel, A. C. 2017, *MNRAS*, **469**, 4359
 Bica, E., Ortolani, S., & Barbuy, B. 1996, *A&AS*, **120**, 153
 Bressan, A., Marigo, P., Girardi, L., Salasnich, B., Dal Cero, C., Rubele, S., & Nanni, A. 2012, *MNRAS*, **427**, 127
 Brodie, J. P., & Strader, J. 2006, *ARA&A*, **44**, 193
 Carraro, G., Janes, K. A., & Eastman, J. D. 2005, *MNRAS*, **364**, 179
 Chambers, K. C., et al. 2016, arXiv e-prints, p. arXiv:1612.05560
 Choi, J., Dotter, A., Conroy, C., Cantiello, M., Paxton, B., & Johnson, B. D. 2016, *ApJ*, **823**, 102
 Cornish, A. S. M., Phelps, R. L., Briley, M. M., & Friel, E. D. 2006, *AJ*, **131**, 2543
 Dalessandro, E., Schiavon, R. P., Rood, R. T., Ferraro, F. R., Sohn, S. T., Lanzoni, B., & O'Connell, R. W. 2012, *AJ*, **144**, 126
 De Boer, T. J. L., Gieles, M., Balbinot, E., Hénault-Brunet, V., Sollima, A., Watkins, L. L., & Claydon, I. 2019, *MNRAS*, **485**, 4906
 Di Criscienzo, M., Caputo, F., Marconi, M., & Musella, I. 2006, *MNRAS*, **365**, 1357
 Dolphin, A. 2016, DOLPHOT: Stellar photometry (ascl:1608.013)
 Dolphin, A. E. 2000, *PASP*, **112**, 1383
 Dotter, A. 2016, *ApJS*, **222**, 8
 Dotter, A., Chaboyer, B., Jevremović, D., Kostov, V., Baron, E., & Ferguson, J. W. 2008a, *ApJS*, **178**, 89
 Dotter, A., Sarajedini, A., & Yang, S.-C. 2008b, *AJ*, **136**, 1407
 Dotter, A., Sarajedini, A., & Anderson, J. 2011, *ApJ*, **738**, 74
 Ferraro, F. R., Messineo, M., Fusi Pecci, F., de Palo, M. A., Straniero, O., Chieffi, A., & Limongi, M. 1999, *AJ*, **118**, 1738
 Fraga, L., Kunder, A., & Tokovinin, A. 2013, *AJ*, **145**, 165
 Frank, M. J., Grebel, E. K., & Küpper, A. H. W. 2014, *MNRAS*, **443**, 815
 Frank, M. J., Hilker, M., Baumgardt, H., Côté, P., Grebel, E. K., Hagh, H., Küpper, A. H. W., & Djorgovski, S. G. 2012, *MNRAS*, **423**, 2917
 Hanes, D. A., & Brodie, J. P. 1985, *MNRAS*, **214**, 491
 Harris, W. E. 1996, *AJ*, **112**, 1487
 Harris, W. E. 2018, *AJ*, **156**, 296
 Harris, W. E., Phelps, R. L., Madore, B. F., Pevunova, O., Skiff Brian, A. Crute, C., Wilson, B., & Archinal, B. A. 1997, *AJ*, **113**, 688
 Hatzidimitriou, D., Papadakis, I., Croke, B. F. W., Papamastorakis, I., Paleologou, E. V., Xanthopoulos, E., & Haerendel, G. 1999, *AJ*, **117**, 3059
 Hilker, M. 2006, *A&A*, **448**, 171
 Holtzman, J. A., et al. 1995, *PASP*, **107**, 156
 Horta, D., et al. 2020, *MNRAS*, **493**, 3363
 Hughes, M. E., Pfeffer, J. L., Martig, M., Reina-Campos, M., Bastian, N., Crain, R. A., & Kruijssen, J. M. D. 2020, *MNRAS*, **491**, 4012
 Huxor, A. P., et al. 2014, *MNRAS*, **442**, 2165
 Inman, R. T., & Carney, B. W. 1987, *AJ*, **93**, 1166
 Kaluzny, J., Krzeminski, W., & Mazur, B. 1995, *AJ*, **110**, 2206
 Kamann, S., et al. 2018, *MNRAS*, **473**, 5591
 Kerber, L. O., Nardiello, D., Ortolani, S., Barbuy, B., Bica, E., Cassisi, S., Libralato, M., & Vieira, R. G. 2018, *ApJ*, **853**, 15
 Kruijssen, J. M. D., et al. 2020, arXiv e-prints, p. arXiv:2003.01119
 Kurucz, R. L. 1992, in IAU Symposium, Vol. 149, The Stellar Populations of Galaxies, ed. B. Barbuy, & A. Renzini, 225
 Lagioia, E. P., et al. 2014, *ApJ*, **782**, 50

- Larsen, S. S., Baumgardt, H., Bastian, N., Hernandez, S., & Brodie, J. 2019, *A&A*, **624**, A25
- Layden, A. C., Bowes, B. T., Welch, D. L., & Webb, T. M. A. 2003, *AJ*, **126**, 255
- Lewis, M. S., Liu, W. M., Paust, N. E. Q., & Chaboyer, B. 2006, *AJ*, **131**, 2538
- Maraston, C. 1999, Synthetic Stellar Mass-to-Light Ratios for Stellar Populations, 28
- Massari, D., Koppelman, H. H., & Helmi, A. 2019, *A&A*, **630**, L4
- McLaughlin, D. E., & van der Marel, R. P. 2005, *ApJS*, **161**, 304
- Minniti, D., et al. 2017, *ApJ*, **838**, L14
- Munoz, R. R., Cote, P., Santana, F. A., Geha, M., Simon, J. D., Oyarzun, G. A., Stetson, P., & Djorgovski, S. G. 2018, arXiv e-prints, p. [arXiv:1806.06889](https://arxiv.org/abs/1806.06889)
- Nardiello, D., et al. 2018, *MNRAS*, **481**, 3382
- Ortolani, S., Barbuy, B., & Bica, E. 1996, *A&A*, **308**, 733
- Ortolani, S., Barbuy, B., & Bica, E. 1997a, *A&A*, **319**, 850
- Ortolani, S., Bica, E., & Barbuy, B. 1995, *A&A*, **296**, 680
- Ortolani, S., Bica, E., & Barbuy, B. 1997b, *A&AS*, **126**, 253
- Ortolani, S., Bica, E., & Barbuy, B. 1997c, *A&A*, **326**, 614
- Ortolani, S., Bica, E., & Barbuy, B. 1998, *A&AS*, **127**, 471
- Ortolani, S., Nardiello, D., Pérez-Villegas, A., Bica, E., & Barbuy, B. 2019a, *A&A*, **622**, A94
- Ortolani, S., et al. 2019b, *A&A*, **627**, A145
- Paxton, B., et al. 2015, *ApJS*, **220**, 15
- Peterson, C. J. 1986, *PASP*, **98**, 192
- Piotto, G., et al. 2002, *A&A*, **391**, 945
- Pota, V., et al. 2015, *MNRAS*, **450**, 3345
- Pritzl, B. J., Venn, K. A., & Irwin, M. 2005, *AJ*, **130**, 2140
- Renzini, A., & Buzzoni, A. 1986, Global properties of stellar populations and the spectral evolution of galaxies, 195, 10.1007/978-94-009-4598-2_19
- Richtler, T., Salinas, R., Misgeld, I., Hilker, M., Hau, G. K. T., Romanowsky, A. J., Schuberth, Y., & Spolaor, M. 2011, *A&A*, **531**, A119
- Rosenberg, A., Piotto, G., Saviane, I., & Aparicio, A. 2000, *A&AS*, **144**, 5
- Sagar, R., Subramaniam, A., Richtler, T., & Grebel, E. K. 1999, *A&AS*, **135**, 391
- Sarajedini, A., et al. 2007, *AJ*, **133**, 1658
- Schlafly, E. F., et al. 2018, *ApJS*, **234**, 39
- Secker, J. 1992, *AJ*, **104**, 1472
- Simpson, J. D. 2018, *MNRAS*, **477**, 4565
- Sirianni, M., et al. 2005, *PASP*, **117**, 1049
- Skrutskie, M. F., et al. 2006, *AJ*, **131**, 1163
- Stetson, P. B. 2000, *PASP*, **112**, 925
- Stetson, P. B. 2020, unpublished, data available from <http://www.cadc.hia.nrc.gc.ca/community/STETSON/>
- Stetson, P. B., et al. 1999, *AJ*, **117**, 247
- Stetson, P. B., Pancino, E., Zocchi, A., Sanna, N., & Monelli, M. 2019, *MNRAS*, **485**, 3042
- Strader, J., Caldwell, N., & Seth, A. C. 2011, *AJ*, **142**, 8
- The Dark Energy Survey Collaboration, 2005, arXiv e-prints, pp [astro-ph/0510346](https://arxiv.org/abs/astro-ph/0510346)
- Trager, S. C., King, I. R., & Djorgovski, S. 1995, *AJ*, **109**, 218
- Valcheva, A. T., Ovcharov, E. P., Lalova, A. D., Nedialkov, P. L., Ivanov, V. D., & Carraro, G. 2015, *MNRAS*, **446**, 730
- VandenBerg, D. A., Brogaard, K., Leaman, R., & Casagrande, L. 2013, *ApJ*, **775**, 134
- Vanderbeke, J., et al. 2014, *MNRAS*, **437**, 1725
- Weisz, D. R., et al. 2016, *ApJ*, **822**, 32
- Wirth, H., Bekki, K., & Hayashi, K. 2020, *MNRAS*,
- Zonoozi, A. H., Hagi, H., & Kroupa, P. 2016, *ApJ*, **826**, 89

A. Input photometry used to derive the apparent magnitudes of globular clusters

Table A.1. Input photometry used to calculate the total magnitudes of globular clusters.

Cluster	Source of photometry	Telescope/Instrument/Band
AM 1	Dotter et al. (2008b)	<i>HST</i> /WFPC2 F555W/F814W
	Hilker (2006)	ESO VLT/FORS2 BV
AM 4	This work	<i>HST</i> /WFC3 F606W/F814W
	Inman & Carney (1987)	CTIO BV
Arp 2	Sarajedini et al. (2007)	<i>HST</i> /ACS F606W/F814W
	Stetson (2020)	Ground-based UBVRI
BH 261	Carraro et al. (2005)	Ground-based BVI
	Schlafly et al. (2018)	Ground-based ugrizY
Crater	Weisz et al. (2016)	<i>HST</i> /ACS F606W/F814W
	Djorg 1	<i>HST</i> /ACS/WFC3 F606W/F160W
Djorg 1	Ortolani et al. (2019a)	ESO NTT VI
	Ortolani, Bica, & Barbuy (1995)	
Djorg 2	Ortolani et al. (2019b)	<i>HST</i> /ACS/WFC3 F606W/F110W
	Ortolani, Bica, & Barbuy (1997b)	Ground-based VI
E 3	Sarajedini et al. (2007)	<i>HST</i> /ACS F606W/F814W
	Stetson et al. (2019)	Ground-based UBVRI
Eridanus	Stetson et al. (1999)	<i>HST</i> /WFPC2 F555W/F814W
	Stetson (2020)	Ground-based UBVRI
	Munoz et al. (2018)	CFHT/MegaCam g/r
ESO 280-SC06	Simpson (2018)	Ground-based VI
ESO 452-SC11	This work	Ground-based VI
FSR 1735	This work	<i>HST</i> /ACS/WFC3 F606W/F110W
FSR 1758	Schlafly et al. (2018)	Ground-based ugrizY
HP 1	Schlafly et al. (2018)	Ground-based ugrizY
	Stetson (2020)	Ground-based UBVRI
IC 1257	This work	Ground-based VI
IC 1276	Stetson (2020)	Ground-based UBVRI
IC 4499	Dotter et al. (2011)	<i>HST</i> /ACS F606W/F814W
	Stetson et al. (2019)	Ground-based UBVRI
Lynga 7	Sarajedini et al. (2007)	<i>HST</i> /ACS F606W/F814W
NGC 104	Sarajedini et al. (2007)	<i>HST</i> /ACS F606W/F814W
	Stetson et al. (2019)	Ground-based UBVRI
NGC 288	Sarajedini et al. (2007)	<i>HST</i> /ACS F606W/F814W
	Stetson et al. (2019)	Ground-based UBVRI
NGC 362	Sarajedini et al. (2007)	<i>HST</i> /ACS F606W/F814W
	Stetson (2020)	Ground-based UBVRI
NGC 1261	Sarajedini et al. (2007)	<i>HST</i> /ACS F606W/F814W
	Stetson et al. (2019)	Ground-based UBVRI
NGC 1851	Sarajedini et al. (2007)	<i>HST</i> /ACS F606W/F814W
	Stetson et al. (2019)	Ground-based UBVRI
NGC 1904	Piotto et al. (2002)	<i>HST</i> /WFPC2 F439W/F555W
	Stetson et al. (2019)	Ground-based UBVRI

Table A.1. continued

Cluster	Source of photometry	Telescope/Instrument/Band
NGC 2298	Sarajedini <i>et al.</i> (2007)	<i>HST</i> /ACS F606W/F814W
	Stetson <i>et al.</i> (2019)	Ground-based UBVR
NGC 2419	Larsen <i>et al.</i> (2019)	<i>HST</i> /ACS F438W/F555W
	Beccari <i>et al.</i> (2013)	LBT, uVI
	Stetson (2020)	Ground-based UBVR
NGC 2808	Sarajedini <i>et al.</i> (2007)	<i>HST</i> /ACS F606W/F814W
	Stetson <i>et al.</i> (2019)	Ground-based UBVR
NGC 3201	Sarajedini <i>et al.</i> (2007)	<i>HST</i> /ACS F606W/F814W
	Stetson <i>et al.</i> (2019)	Ground-based UBVR
NGC 4147	Sarajedini <i>et al.</i> (2007)	<i>HST</i> /ACS F606W/F814W
	Stetson <i>et al.</i> (2019)	Ground-based UBVR
NGC 4372	Piotto <i>et al.</i> (2002)	<i>HST</i> /WFPC2 F439W/F555W
	Stetson <i>et al.</i> (2019)	Ground-based UBVR
NGC 4590	Sarajedini <i>et al.</i> (2007)	<i>HST</i> /ACS F606W/F814W
	Stetson <i>et al.</i> (2019)	Ground-based UBVR
NGC 4833	Sarajedini <i>et al.</i> (2007)	<i>HST</i> /ACS F606W/F814W
	Stetson <i>et al.</i> (2019)	Ground-based UBVR
NGC 5024	Sarajedini <i>et al.</i> (2007)	<i>HST</i> /ACS F606W/F814W
	Stetson <i>et al.</i> (2019)	Ground-based UBVR
NGC 5053	Sarajedini <i>et al.</i> (2007)	<i>HST</i> /ACS F606W/F814W
	Stetson <i>et al.</i> (2019)	Ground-based UBVR
NGC 5139	Sarajedini <i>et al.</i> (2007)	<i>HST</i> /ACS F606W/F814W
	Stetson <i>et al.</i> (2019)	Ground-based UBVR
NGC 5272	Sarajedini <i>et al.</i> (2007)	<i>HST</i> /ACS F606W/F814W
	Stetson <i>et al.</i> (2019)	Ground-based UBVR
NGC 5286	Sarajedini <i>et al.</i> (2007)	<i>HST</i> /ACS F606W/F814W
	Stetson <i>et al.</i> (2019)	Ground-based UBVR
NGC 5466	Sarajedini <i>et al.</i> (2007)	<i>HST</i> /ACS F606W/F814W
	Stetson (2020)	Ground-based UBVR
NGC 5634	Piotto <i>et al.</i> (2002)	<i>HST</i> /WFPC2 F439W/F555W
	Stetson <i>et al.</i> (2019)	Ground-based UBVR
NGC 5694	Piotto <i>et al.</i> (2002)	<i>HST</i> /WFPC2 F439W/F555W
	Stetson <i>et al.</i> (2019)	Ground-based UBVR
NGC 5824	Piotto <i>et al.</i> (2002)	<i>HST</i> /WFPC2 F439W/F555W
	Stetson <i>et al.</i> (2019)	Ground-based UBVR
NGC 5897	Nardiello <i>et al.</i> (2018)	<i>HST</i> /WFC3 F606W/F814W
	Stetson (2020)	Ground-based UBVR
NGC 5904	Sarajedini <i>et al.</i> (2007)	<i>HST</i> /ACS F606W/F814W
	Stetson <i>et al.</i> (2019)	Ground-based UBVR
NGC 5927	Sarajedini <i>et al.</i> (2007)	<i>HST</i> /ACS F606W/F814W
	Stetson <i>et al.</i> (2019)	Ground-based UBVR
NGC 5946	Baumgardt <i>et al.</i> (2019)	<i>HST</i> /WFC3 F438W/F555W
	Alcaino <i>et al.</i> (1991)	Ground-based BV
NGC 5986	Sarajedini <i>et al.</i> (2007)	<i>HST</i> /ACS F606W/F814W
	Stetson <i>et al.</i> (2019)	Ground-based UBVR
NGC 6093	Sarajedini <i>et al.</i> (2007)	<i>HST</i> /ACS F606W/F814W
	Stetson (2020)	Ground-based UBVR
NGC 6101	Sarajedini <i>et al.</i> (2007)	<i>HST</i> /ACS F606W/F814W
	Stetson <i>et al.</i> (2019)	Ground-based UBVR

Table A.1. continued

Cluster	Source of photometry	Telescope/Instrument/Band
NGC 6121	Sarajedini <i>et al.</i> (2007)	<i>HST</i> /ACS F606W/F814W
	Stetson <i>et al.</i> (2019)	Ground-based UBVR
NGC 6139	Baumgardt <i>et al.</i> (2019)	<i>HST</i> /WFC3 F438W/F555W
	Stetson (2020)	Ground-based UBVR
NGC 6144	Sarajedini <i>et al.</i> (2007)	<i>HST</i> /ACS F606W/F814W
	Stetson (2020)	Ground-based UBVR
NGC 6171	Sarajedini <i>et al.</i> (2007)	<i>HST</i> /ACS F606W/F814W
	Stetson (2020)	Ground-based UBVR
NGC 6205	Sarajedini <i>et al.</i> (2007)	<i>HST</i> /ACS F606W/F814W
	Stetson <i>et al.</i> (2019)	Ground-based UBVR
NGC 6218	Sarajedini <i>et al.</i> (2007)	<i>HST</i> /ACS F606W/F814W
	Stetson <i>et al.</i> (2019)	Ground-based UBVR
NGC 6229	Piotto <i>et al.</i> (2002)	<i>HST</i> /WFPC2 F439W/F555W
	Stetson (2020)	Ground-based UBVR
NGC 6235	Piotto <i>et al.</i> (2002)	<i>HST</i> /WFPC2 F439W/F555W
	Stetson (2020)	Ground-based UBVR
NGC 6254	Sarajedini <i>et al.</i> (2007)	<i>HST</i> /ACS F606W/F814W
	Stetson <i>et al.</i> (2019)	Ground-based UBVR
NGC 6256	Baumgardt <i>et al.</i> (2019)	<i>HST</i> /WFC3 F555W/F814W
	Stetson (2020)	Ground-based UBVR
NGC 6266	Piotto <i>et al.</i> (2002)	<i>HST</i> /WFPC2 F439W/F555W
	Stetson (2020)	Ground-based UBVR
NGC 6273	Baumgardt <i>et al.</i> (2019)	<i>HST</i> /WFC3 F555W/F814W
	Stetson (2020)	Ground-based UBVR
NGC 6284	Piotto <i>et al.</i> (2002)	<i>HST</i> /WFPC2 F439W/F555W
	Stetson (2020)	Ground-based UBVR
NGC 6287	Piotto <i>et al.</i> (2002)	<i>HST</i> /WFPC2 F439W/F555W
	Stetson (2020)	Ground-based UBVR
NGC 6293	Kamann <i>et al.</i> (2018)	<i>HST</i> /WFC3 F555W/F814W
	NGC 6304	Sarajedini <i>et al.</i> (2007)
NGC 6316	Rosenberg <i>et al.</i> (2000)	ESO Dutch Telescope VI
	Piotto <i>et al.</i> (2002)	<i>HST</i> /WFPC2 F439W/F555W
NGC 6325	Layden <i>et al.</i> (2003)	CTIO VI
	Baumgardt <i>et al.</i> (2019)	<i>HST</i> /WFC3 F438W/F555W
NGC 6325	Stetson (2020)	Ground-based UBVR
	Baumgardt <i>et al.</i> (2019)	<i>HST</i> /ACS F435W/F555W
NGC 6333	Stetson (2020)	Ground-based UBVR
	NGC 6341	Sarajedini <i>et al.</i> (2007)
NGC 6342	Stetson <i>et al.</i> (2019)	Ground-based UBVR
	Baumgardt <i>et al.</i> (2019)	<i>HST</i> /WFC3 F438W/F555W
NGC 6342	Stetson <i>et al.</i> (2019)	Ground-based UBVR
	NGC 6352	Sarajedini <i>et al.</i> (2007)
NGC 6352	Stetson (2020)	Ground-based UBVR
	NGC 6355	Baumgardt <i>et al.</i> (2019)
NGC 6356	Piotto <i>et al.</i> (2002)	<i>HST</i> /WFPC2 F439W/F555W
	Stetson (2020)	Ground-based UBVR
NGC 6362	Sarajedini <i>et al.</i> (2007)	<i>HST</i> /ACS F606W/F814W
	Stetson (2020)	Ground-based UBVR

Table A.1. continued

Cluster	Source of photometry	Telescope/Instrument/Band
NGC 6366	Sarajedini et al. (2007)	HST/ACS F606W/F814W
	Stetson et al. (2019)	Ground-based UBVRI
NGC 6380	Baumgardt et al. (2019)	HST/WFC3 F555W/F814W
	Ortolani et al. (1998)	ESO NTT VI
NGC 6388	Sarajedini et al. (2007)	HST/ACS F606W/F814W
	Stetson (2020)	Ground-based UBVRI
NGC 6397	Sarajedini et al. (2007)	HST/ACS F606W/F814W
	Stetson (2020)	Ground-based UBVRI
NGC 6401	This work	HST/ACS F606W/F814W
	Stetson (2020)	Ground-based UBVRI
NGC 6402	Piotto et al. (2002)	HST/WFPC2 F439W/F555W
	Stetson (2020)	Ground-based UBVRI
NGC 6426	Dotter et al. (2011)	HST/ACS F606W/F814W
	Hatzidimitriou et al. (1999)	Ground-based BVRI
NGC 6440	Stetson (2020)	Ground-based UBVRI
NGC 6441	Sarajedini et al. (2007)	HST/ACS F606W/F814W
	Stetson (2020)	Ground-based UBVRI
NGC 6453	Baumgardt et al. (2019)	HST/WFC3 F438W/F555W
NGC 6496	Sarajedini et al. (2007)	HST/ACS F606W/F814W
	Fraga et al. (2013)	Ground-based BVRI
NGC 6517	Baumgardt et al. (2019)	HST/WFC3 F555W/F814W
	Stetson (2020)	Ground-based UBVRI
NGC 6522	Kamann et al. (2018)	HST/WFC3 F555W/F814W
	Stetson (2020)	Ground-based UBVRI
NGC 6528	Lagioia et al. (2014)	HST/ACS F606W/F814W
	Stetson (2020)	Ground-based UBVRI
NGC 6535	Sarajedini et al. (2007)	HST/ACS F606W/F814W
	Stetson (2020)	Ground-based UBVRI
NGC 6539	Piotto et al. (2002)	HST/WFPC2 F439W/F555W
	Stetson (2020)	Ground-based UBVRI
NGC 6540	Piotto et al. (2002)	HST/WFPC2 F439W/F555W
	Schlafly et al. (2018)	Ground-based ugrizY
NGC 6541	Sarajedini et al. (2007)	HST/ACS F606W/F814W
	Stetson (2020)	Ground-based UBVRI
NGC 6544	Piotto et al. (2002)	HST/WFPC2 F439W/F555W
	Rosenberg et al. (2000)	ESO Dutch Telescope VI
NGC 6553	Beaulieu et al. (2001)	HST/WFPC2 F555W/F814W
	Sagar et al. (1999)	Ground-based VI
NGC 6558	Stetson (2020)	Ground-based UBVRI
NGC 6569	Piotto et al. (2002)	HST/WFPC2 F439W/F555W
	Stetson (2020)	Ground-based UBVRI
NGC 6584	Sarajedini et al. (2007)	HST/ACS F606W/F814W
	Stetson (2020)	Ground-based UBVRI
NGC 6624	Sarajedini et al. (2007)	HST/ACS F606W/F814W
	Rosenberg et al. (2000)	ESO Dutch Telescope VI
NGC 6626	Kerber et al. (2018)	HST/ACS F435W/F625W
	Stetson (2020)	Ground-based UBVRI

Table A.1. continued

Cluster	Source of photometry	Telescope/Instrument/Band
NGC 6637	Sarajedini et al. (2007)	HST/ACS F606W/F814W
	Stetson (2020)	Ground-based UBVRI
NGC 6638	Piotto et al. (2002)	HST/WFPC2 F439W/F555W
	Rosenberg et al. (2000)	ESO Dutch Telescope VI
NGC 6642	Baumgardt et al. (2019)	HST/ACS F606W/F814W
	Stetson (2020)	Ground-based UBVRI
NGC 6652	Sarajedini et al. (2007)	HST/ACS F606W/F814W
NGC 6656	Sarajedini et al. (2007)	HST/ACS F606W/F814W
	Stetson et al. (2019)	Ground-based UBVRI
NGC 6681	Sarajedini et al. (2007)	HST/ACS F606W/F814W
NGC 6712	Stetson (2020)	Ground-based UBVRI
	Piotto et al. (2002)	HST/WFPC2 F439W/F555W
NGC 6715	Stetson et al. (2019)	Ground-based UBVRI
	Sarajedini et al. (2007)	HST/ACS F606W/F814W
NGC 6717	Stetson (2020)	Ground-based UBVRI
	Sarajedini et al. (2007)	HST/ACS F606W/F814W
NGC 6723	Stetson (2020)	Ground-based UBVRI
	Sarajedini et al. (2007)	HST/ACS F606W/F814W
NGC 6749	Stetson (2020)	Ground-based UBVRI
	Sarajedini et al. (2007)	HST/ACS F606W/F814W
NGC 6752	Stetson et al. (2019)	Ground-based UBVRI
	Sarajedini et al. (2007)	HST/ACS F606W/F814W
NGC 6760	Baumgardt et al. (2019)	HST/ACS F336W/F625W
	Stetson et al. (2019)	Ground-based UBVRI
NGC 6779	Sarajedini et al. (2007)	HST/ACS F606W/F814W
	Stetson (2020)	Ground-based UBVRI
NGC 6809	Sarajedini et al. (2007)	HST/ACS F606W/F814W
	Stetson et al. (2019)	Ground-based UBVRI
NGC 6838	Sarajedini et al. (2007)	HST/ACS F606W/F814W
	Stetson et al. (2019)	Ground-based UBVRI
NGC 6864	Baumgardt et al. (2019)	HST/WFC3 F438W/F555W
	Stetson (2020)	Ground-based UBVRI
NGC 6934	Sarajedini et al. (2007)	HST/ACS F606W/F814W
	Stetson et al. (2019)	Ground-based UBVRI
NGC 6981	Sarajedini et al. (2007)	HST/ACS F606W/F814W
	Stetson et al. (2019)	Ground-based UBVRI
NGC 7006	Dotter et al. (2011)	HST/ACS F606W/F814W
	Stetson et al. (2019)	Ground-based UBVRI
NGC 7078	Sarajedini et al. (2007)	HST/ACS F606W/F814W
NGC 7089	Stetson et al. (2019)	Ground-based UBVRI
	Sarajedini et al. (2007)	HST/ACS F606W/F814W
NGC 7099	Stetson et al. (2019)	Ground-based UBVRI
	Sarajedini et al. (2007)	HST/ACS F606W/F814W
NGC 7492	Stetson et al. (2019)	Ground-based UBVRI
	Sarajedini et al. (2007)	HST/ACS F606W/F814W
Pal 1	Stetson (2020)	Ground-based UBVRI

Table A.1. continued

Cluster	Source of photometry	Telescope/Instrument/Band
Pal 2	Sarajedini <i>et al.</i> (2007)	<i>HST</i> /ACS F606W/F814W
	Stetson (2020)	Ground-based UBVRI
Pal 3	Stetson <i>et al.</i> (1999)	<i>HST</i> /WFPC2 F555W/F814W
	Stetson (2020)	Ground-based UBVRI
Pal 4	Frank <i>et al.</i> (2012)	<i>HST</i> /WFPC2 F555W/F814W
	Stetson (2020)	Ground-based UBVRI
Pal 5	Stetson (2020)	Ground-based UBVRI
Pal 6	Ortolani <i>et al.</i> (1995)	Ground-based VI
	Schlafly <i>et al.</i> (2018)	Ground-based ugrizY
Pal 10	Stetson (2020)	Ground-based UBVRI
Pal 11	Lewis <i>et al.</i> (2006)	KPNO/Hiltner V/I
	Stetson (2020)	Ground-based UBVRI
Pal 12	Sarajedini <i>et al.</i> (2007)	<i>HST</i> /ACS F606W/F814W
	Stetson (2020)	Ground-based UBVRI
Pal 13	This work	<i>HST</i> /WFC3 F606W/F814W
	Stetson (2020)	Ground-based UBVRI
Pal 14	Frank <i>et al.</i> (2014)	<i>HST</i> /WFPC2 F555W/F814W
	Stetson (2020)	Ground-based UBVRI
Pal 15	Dotter <i>et al.</i> (2011)	<i>HST</i> /ACS F606W/F814W
	Stetson (2020)	Ground-based UBVRI
Pyxis	Dotter <i>et al.</i> (2011)	<i>HST</i> /ACS F606W/F814W
	Stetson (2020)	Ground-based UBVRI
Rup 106	Dotter <i>et al.</i> (2011)	<i>HST</i> /ACS F606W/F814W
	Kaluzny <i>et al.</i> (1995)	Ground-based BV
Sgr 2	This work	<i>HST</i> /ACS F606W/F814W
	Munoz <i>et al.</i> (2018)	CFHT/MegaCam g/r
Ter 1	Schlafly <i>et al.</i> (2018)	Ground-based ugrizY
Ter 2	Ortolani <i>et al.</i> (1997c)	Ground-based VI
Ter 3	This work	<i>HST</i> /ACS F625W/F658N
Ter 4	Ortolani <i>et al.</i> (1997a)	Ground-based VI
Ter 5	Ortolani <i>et al.</i> (1996)	Ground-based VI
Ter 6	Barbuy <i>et al.</i> (1997)	Ground-based VI
Ter 7	Sarajedini <i>et al.</i> (2007)	<i>HST</i> /ACS F606W/F814W
	Stetson (2020)	Ground-based UBVRI
Ter 8	Sarajedini <i>et al.</i> (2007)	<i>HST</i> /ACS F606W/F814W
	Stetson (2020)	Ground-based UBVRI
Ter 9	Schlafly <i>et al.</i> (2018)	Ground-based ugrizY
Ter 10	Ortolani <i>et al.</i> (2019a)	<i>HST</i> /ACS/WFC3 F606W/F160W
	Ortolani <i>et al.</i> (1997b)	Ground-based VI
Ter 12	Ortolani <i>et al.</i> (1998)	Ground-based VI
Ton 2	Bica <i>et al.</i> (1996)	Ground-based VI
	Schlafly <i>et al.</i> (2018)	Ground-based ugrizY
Whiting 1	Valcheva <i>et al.</i> (2015)	ESO NTT V/I

B. Derived magnitudes and mass-to-light ratios

Table B.1. Apparent and absolute V -band magnitudes, mass-to-light ratios, and the radii containing 10% and half the total cluster light in projection together with the surface density brightnesses at these radii for all clusters in this study.

Name	V_{Tot} (mag)	M_V (mag)	M/L_V (M_{\odot}/L_{\odot})	r_{10} (")	r_H (")	$\mu_{V,10}$ (mag arcsec $^{-2}$)	$\mu_{V,H}$ (mag arcsec $^{-2}$)
AM 1	15.07 ± 0.07	-6.19	0.85 ± 0.18	7.2	24.2	23.39	25.12
AM 4	16.49 ± 0.08	-1.20	3.38 ± 0.73	10.5	46.1	27.27	28.60
Arp 2	11.65 ± 0.07	-5.94	1.91 ± 0.35	33.5	111.7	22.89	24.81
BH 140	9.14 ± 0.11	-6.21	1.88 ± 0.31	87.1	263.7	22.73	24.16
BH 261	10.75 ± 0.15	-4.43	1.89 ± 0.32	19.2	92.9	21.76	25.04
Crater	15.74 ± 0.06	-5.07	1.18 ± 0.24	9.1	27.2	24.12	25.98
Djor 1	13.08 ± 0.22	-6.66	1.88 ± 0.56	19.7	86.8	23.41	25.02
Djor 2	10.70 ± 0.19	-6.52	2.29 ± 0.45	18.0	71.3	21.36	22.60
E 3	11.84 ± 0.05	-3.62	1.20 ± 0.24	31.8	111.2	23.72	24.68
Eridanus	15.02 ± 0.06	-5.56	0.67 ± 0.14	10.1	33.6	24.02	25.53
ESO 280	12.51 ± 0.09	-4.28	1.69 ± 0.44	17.6	69.6	22.45	24.70
ESO 452	11.77 ± 0.09	-3.82	2.70 ± 1.43	18.2	67.5	21.05	24.83
FSR 1716	13.05 ± 0.16	-4.82	2.18 ± 2.53	37.2	120.0	24.76	26.07
FSR 1735	14.38 ± 0.09	-7.09	1.33 ± 0.29	11.8	44.4	24.08	25.50
FSR 1758	9.14 ± 0.11	-8.96	1.79 ± 0.31	88.3	235.0	22.37	23.63
HP 1	11.07 ± 0.19	-6.56	2.91 ± 0.90	21.9	75.9	21.74	23.44
IC 1257	13.81 ± 0.18	-5.44	1.55 ± 0.42	5.6	30.2	20.91	24.35
IC 1276	9.93 ± 0.09	-7.08	1.43 ± 0.41	43.3	160.3	22.15	24.08
IC 4499	9.84 ± 0.08	-7.18	2.03 ± 0.42	31.8	110.5	21.22	22.85
Lil 1	15.73 ± 0.09	-9.04	2.46 ± 0.45	5.1	26.2	23.26	26.16
Lynga 7	9.87 ± 0.16	-6.91	2.06 ± 0.55	34.5	107.6	21.49	22.40
NGC 104	4.08 ± 0.08	-9.28	1.89 ± 0.14	26.8	168.5	15.40	18.79
NGC 288	8.09 ± 0.07	-6.77	2.14 ± 0.15	46.9	143.6	20.38	21.69
NGC 362	6.48 ± 0.06	-8.49	1.46 ± 0.08	10.9	51.1	15.75	18.40
NGC 1261	8.31 ± 0.06	-7.77	1.62 ± 0.10	10.7	41.1	17.61	19.25
NGC 1851	7.07 ± 0.07	-8.26	1.63 ± 0.11	5.1	30.6	15.06	17.74
NGC 1904	7.94 ± 0.07	-7.65	1.47 ± 0.15	7.8	40.1	16.69	19.11
NGC 2298	9.06 ± 0.05	-6.54	1.63 ± 0.34	12.6	50.3	18.69	20.99
NGC 2419	10.56 ± 0.07	-9.29	2.05 ± 0.34	12.3	46.8	20.11	22.00
NGC 2808	6.14 ± 0.06	-9.59	1.52 ± 0.09	11.1	50.6	15.58	17.73
NGC 3201	6.77 ± 0.07	-7.29	2.01 ± 0.13	39.2	166.4	19.40	21.11
NGC 4147	10.29 ± 0.05	-6.07	1.66 ± 0.41	5.4	28.6	18.69	21.02
NGC 4372	7.37 ± 0.07	-7.64	2.10 ± 0.18	68.4	188.7	20.57	21.65
NGC 4590	8.00 ± 0.07	-7.19	2.01 ± 0.22	24.2	89.0	19.01	20.85
NGC 4833	7.19 ± 0.05	-7.89	1.36 ± 0.11	30.2	104.5	18.51	20.23
NGC 5024	7.71 ± 0.06	-8.62	1.74 ± 0.17	17.0	72.6	17.68	20.06
NGC 5053	9.93 ± 0.06	-6.28	2.60 ± 0.59	53.2	146.0	22.02	23.21
NGC 5139	3.50 ± 0.06	-10.47	2.46 ± 0.15	90.0	284.9	17.23	18.58
NGC 5272	6.38 ± 0.06	-8.56	1.64 ± 0.12	16.3	69.4	16.64	18.71
NGC 5286	7.35 ± 0.06	-8.69	1.42 ± 0.09	10.2	44.8	16.25	18.78
NGC 5466	9.32 ± 0.06	-6.70	1.44 ± 0.30	41.2	123.1	21.46	22.26

Table B.1. continued

Name	V_{Tot} (mag)	M_V (mag)	M/L_V (M_{\odot}/L_{\odot})	r_{10} (")	r_H (")	$\mu_{V,10}$ (mag arcsec $^{-2}$)	$\mu_{V,H}$ (mag arcsec $^{-2}$)
NGC 5634	9.51 ± 0.11	−7.82	1.91 ± 0.46	6.4	36.1	18.16	20.73
NGC 5694	9.87 ± 0.18	−8.27	2.08 ± 0.42	2.6	18.6	16.56	19.47
NGC 5824	8.86 ± 0.10	−9.05	2.17 ± 0.24	5.0	29.8	16.38	19.74
NGC 5897	8.48 ± 0.06	−7.30	2.19 ± 0.29	43.0	126.0	20.81	21.66
NGC 5904	5.95 ± 0.05	−8.54	1.62 ± 0.08	23.3	97.2	16.79	19.06
NGC 5927	7.74 ± 0.07	−8.45	1.58 ± 0.10	23.5	86.4	18.52	20.67
NGC 5946	9.50 ± 0.13	−7.31	1.89 ± 0.41	9.0	41.4	18.53	21.00
NGC 5986	7.71 ± 0.06	−8.28	1.89 ± 0.18	15.1	54.9	17.95	19.48
NGC 6093	7.42 ± 0.05	−8.13	1.93 ± 0.12	7.8	35.4	15.99	18.39
NGC 6101	8.68 ± 0.05	−7.02	2.35 ± 0.66	43.2	138.1	20.64	22.12
NGC 6121	5.66 ± 0.07	−6.86	1.97 ± 0.13	59.9	279.4	18.54	20.97
NGC 6139	8.97 ± 0.12	−8.31	1.92 ± 0.37	7.9	41.8	18.04	20.34
NGC 6144	9.25 ± 0.06	−6.62	1.66 ± 0.46	28.0	92.2	20.63	22.29
NGC 6171	8.28 ± 0.06	−6.63	2.11 ± 0.17	28.0	104.9	19.17	21.41
NGC 6205	5.81 ± 0.07	−8.40	2.32 ± 0.18	28.8	97.5	17.02	18.67
NGC 6218	7.08 ± 0.07	−6.85	1.85 ± 0.14	32.2	115.4	18.81	20.15
NGC 6229	9.33 ± 0.08	−8.13	1.89 ± 0.63	5.6	21.6	17.05	19.23
NGC 6235	9.62 ± 0.07	−6.99	2.10 ± 0.68	14.9	57.5	19.40	21.44
NGC 6254	6.62 ± 0.07	−7.73	1.80 ± 0.12	31.4	123.0	17.91	20.20
NGC 6256	10.55 ± 0.16	−6.85	2.43 ± 0.85	15.1	79.3	20.93	23.36
NGC 6266	6.60 ± 0.09	−8.89	2.00 ± 0.18	12.4	58.4	16.44	18.74
NGC 6273	6.88 ± 0.07	−8.89	2.15 ± 0.17	19.5	78.3	17.42	19.35
NGC 6284	9.31 ± 0.14	−7.46	1.53 ± 0.39	8.1	43.6	18.31	20.97
NGC 6287	9.27 ± 0.10	−7.46	1.88 ± 0.44	11.0	50.0	19.12	20.72
NGC 6293	8.40 ± 0.16	−7.41	1.75 ± 0.31	19.3	53.5	17.97	20.28
NGC 6304	8.18 ± 0.10	−7.30	1.94 ± 0.25	13.1	66.9	17.89	20.63
NGC 6316	9.02 ± 0.26	−7.98	2.17 ± 0.71	9.8	55.2	18.02	21.33
NGC 6325	10.89 ± 0.10	−6.39	2.78 ± 0.53	9.7	46.9	19.66	22.31
NGC 6333	7.65 ± 0.07	−8.15	2.08 ± 0.21	17.6	68.4	17.90	19.93
NGC 6341	6.50 ± 0.05	−8.19	1.92 ± 0.10	14.0	58.2	16.35	18.30
NGC 6342	9.86 ± 0.14	−6.19	2.47 ± 0.55	7.9	38.7	18.73	21.35
NGC 6352	8.06 ± 0.07	−6.24	2.14 ± 0.17	27.0	109.6	19.37	21.35
NGC 6355	10.04 ± 0.11	−7.17	1.91 ± 0.35	11.4	56.2	19.30	22.12
NGC 6356	8.32 ± 0.10	−8.45	2.13 ± 0.50	11.8	51.6	19.08	20.51
NGC 6362	7.45 ± 0.07	−7.16	1.87 ± 0.14	44.3	139.2	19.21	21.10
NGC 6366	8.85 ± 0.07	−6.24	1.51 ± 0.19	67.6	218.8	21.78	23.42
NGC 6380	10.70 ± 0.18	−7.88	1.97 ± 0.50	16.4	68.4	20.83	23.46
NGC 6388	6.81 ± 0.06	−9.49	2.15 ± 0.12	7.9	49.6	15.70	18.73
NGC 6397	5.45 ± 0.06	−7.05	1.58 ± 0.10	30.2	181.7	17.79	20.37
NGC 6401	9.91 ± 0.13	−6.76	3.19 ± 1.69	13.4	57.9	19.46	21.74
NGC 6402	7.87 ± 0.09	−8.84	1.91 ± 0.24	25.7	72.1	18.82	20.11
NGC 6426	11.13 ± 0.07	−6.47	1.95 ± 0.81	15.6	52.4	21.01	22.79
NGC 6440	8.98 ± 0.19	−8.92	1.58 ± 0.36	6.9	32.2	17.60	19.81
NGC 6441	7.12 ± 0.12	−9.70	1.94 ± 0.24	6.9	35.0	15.87	18.29
NGC 6453	9.19 ± 0.19	−8.12	1.39 ± 0.34	10.7	71.1	18.56	21.75
NGC 6496	8.64 ± 0.14	−6.62	1.70 ± 0.34	30.1	93.3	20.29	21.59

Table B.1. continued

Name	V_{Tot} (mag)	M_V (mag)	M/L_V (M_{\odot}/L_{\odot})	r_{10} (")	r_H (")	$\mu_{V,10}$ (mag arcsec $^{-2}$)	$\mu_{V,H}$ (mag arcsec $^{-2}$)
NGC 6517	10.70 ± 0.09	-7.78	2.27 ± 0.67	6.8	37.9	19.43	21.98
NGC 6522	8.14 ± 0.07	-7.86	1.97 ± 0.18	14.0	71.0	17.79	20.99
NGC 6528	9.71 ± 0.15	-6.32	1.69 ± 0.31	7.8	50.0	18.51	21.49
NGC 6535	10.10 ± 0.06	-5.02	1.52 ± 0.25	16.4	86.9	20.79	23.46
NGC 6539	9.95 ± 0.07	-7.69	2.15 ± 0.29	25.4	93.9	21.09	22.69
NGC 6540	9.74 ± 0.17	-5.89	1.97 ± 0.70	10.6	70.9	20.09	22.57
NGC 6541	6.62 ± 0.06	-8.32	1.38 ± 0.09	10.1	63.1	16.16	19.12
NGC 6544	7.86 ± 0.32	-6.58	2.33 ± 0.84	21.1	124.7	19.24	21.36
NGC 6553	8.04 ± 0.09	-7.80	2.50 ± 0.26	21.8	88.2	18.78	20.91
NGC 6558	9.66 ± 0.17	-6.00	1.82 ± 0.50	11.7	45.1	18.94	21.22
NGC 6569	8.89 ± 0.12	-7.75	1.99 ± 0.30	14.0	50.8	18.69	20.58
NGC 6584	8.76 ± 0.05	-7.30	1.14 ± 0.38	14.8	52.5	18.60	20.23
NGC 6624	8.04 ± 0.11	-7.18	1.50 ± 0.16	9.3	58.7	17.18	20.23
NGC 6626	6.85 ± 0.10	-8.06	2.01 ± 0.21	13.1	61.9	16.68	18.99
NGC 6637	7.62 ± 0.06	-7.54	1.83 ± 0.22	14.0	55.3	17.22	19.56
NGC 6638	8.79 ± 0.15	-7.55	1.34 ± 0.35	9.4	39.5	17.45	20.02
NGC 6642	9.65 ± 0.13	-6.30	2.27 ± 0.53	6.9	34.8	18.04	20.79
NGC 6652	8.92 ± 0.06	-6.36	1.72 ± 0.31	6.2	32.0	17.13	19.48
NGC 6656	5.06 ± 0.07	-8.54	1.83 ± 0.13	47.0	198.9	17.63	19.65
NGC 6681	7.91 ± 0.06	-7.16	1.84 ± 0.11	8.0	47.5	17.13	19.56
NGC 6712	8.59 ± 0.07	-7.01	1.71 ± 0.16	20.6	71.4	19.51	20.56
NGC 6715	7.57 ± 0.10	-9.81	2.06 ± 0.20	4.7	28.3	15.38	18.26
NGC 6717	8.98 ± 0.06	-5.59	1.70 ± 0.40	17.1	109.6	18.90	22.63
NGC 6723	7.21 ± 0.06	-7.54	1.96 ± 0.17	26.5	88.2	18.07	19.84
NGC 6749	10.90 ± 0.10	-8.21	1.34 ± 0.60	30.9	131.4	22.94	24.74
NGC 6752	5.34 ± 0.08	-7.92	2.09 ± 0.17	24.2	146.1	16.56	19.41
NGC 6760	8.89 ± 0.08	-8.00	1.89 ± 0.27	17.7	79.4	19.07	21.72
NGC 6779	8.15 ± 0.08	-7.59	1.67 ± 0.22	16.1	59.1	18.28	20.09
NGC 6809	6.29 ± 0.06	-7.58	2.07 ± 0.13	56.0	177.7	18.79	20.12
NGC 6838	7.16 ± 0.05	-6.62	1.35 ± 0.09	44.0	173.1	19.52	21.74
NGC 6864	8.50 ± 0.06	-8.66	1.63 ± 0.34	4.2	20.9	15.89	18.39
NGC 6934	8.75 ± 0.06	-7.50	1.77 ± 0.30	10.4	39.0	17.58	19.90
NGC 6981	9.32 ± 0.06	-6.99	1.60 ± 0.31	16.0	51.7	18.88	20.66
NGC 7006	10.69 ± 0.06	-7.54	1.52 ± 0.40	6.0	23.0	18.48	20.48
NGC 7078	6.29 ± 0.10	-9.07	1.55 ± 0.15	5.3	39.6	14.75	17.74
NGC 7089	6.47 ± 0.06	-8.82	1.78 ± 0.11	11.8	48.9	16.15	18.26
NGC 7099	7.37 ± 0.07	-7.24	2.04 ± 0.17	9.4	62.7	17.00	19.65
NGC 7492	11.14 ± 0.05	-5.98	1.40 ± 0.41	21.3	64.4	22.09	22.89
Pal 1	13.95 ± 0.05	-1.72	2.45 ± 0.49	8.1	33.6	22.92	25.46
Pal 2	12.64 ± 0.09	-8.38	1.22 ± 0.53	9.2	38.5	21.46	23.62
Pal 3	14.52 ± 0.06	-5.44	1.08 ± 0.20	15.1	43.9	24.64	25.49
Pal 4	14.23 ± 0.07	-5.90	1.41 ± 0.61	12.4	35.0	23.49	24.65
Pal 5	11.86 ± 0.07	-4.90	1.90 ± 0.34	68.4	192.8	25.29	26.16
Pal 6	11.60 ± 0.13	-6.74	2.29 ± 0.77	20.1	78.9	21.76	24.03
Pal 10	12.37 ± 0.05	-6.63	1.72 ± 0.95	26.9	98.4	23.29	25.19

Table B.1. continued

Name	V_{Tot} (mag)	M_V (mag)	M/L_V (M_{\odot}/L_{\odot})	r_{10} (")	r_H (")	$\mu_{V,10}$ (mag arcsec $^{-2}$)	$\mu_{V,H}$ (mag arcsec $^{-2}$)
Pal 11	11.86 ± 0.05	-5.16	1.13 ± 0.49	28.8	85.4	22.86	24.05
Pal 12	11.99 ± 0.07	-4.47	1.21 ± 0.25	23.1	76.5	23.10	24.79
Pal 13	13.89 ± 0.08	-3.27	1.74 ± 0.35	20.5	113.4	24.52	27.90
Pal 14	14.13 ± 0.06	-5.22	1.74 ± 0.34	23.5	68.6	24.62	26.50
Pal 15	13.55 ± 0.08	-5.77	2.94 ± 0.62	32.9	93.2	24.67	25.97
Pyxis	13.21 ± 0.07	-5.64	1.71 ± 0.31	34.8	96.4	24.31	26.43
Rup 106	11.05 ± 0.05	-6.20	1.34 ± 0.24	25.8	76.2	22.44	22.90
Sgr 2	14.04 ± 0.12	-5.62	1.35 ± 0.29	30.5	90.5	24.23	26.30
Ter 1	12.41 ± 0.11	-7.89	1.70 ± 0.34	13.0	52.6	22.20	24.16
Ter 2	13.11 ± 0.15	-7.06	1.92 ± 1.07	12.6	67.6	22.89	25.27
Ter 3	10.59 ± 0.21	-6.22	2.15 ± 0.89	40.6	124.9	23.36	99.99
Ter 4	13.43 ± 0.39	-7.06	2.32 ± 1.09	34.4	156.2	25.31	99.99
Ter 5	12.36 ± 0.12	-8.72	3.15 ± 0.41	10.8	52.7	21.65	24.17
Ter 6	14.47 ± 0.10	-6.95	2.29 ± 0.98	7.2	50.6	22.94	26.40
Ter 7	11.86 ± 0.07	-5.15	1.98 ± 0.37	15.8	54.1	20.71	23.63
Ter 8	11.04 ± 0.05	-6.46	1.79 ± 0.41	38.1	114.4	22.90	23.78
Ter 9	12.73 ± 0.12	-6.56	2.30 ± 0.42	11.8	57.8	21.78	25.11
Ter 10	14.73 ± 0.16	-7.07	5.27 ± 1.34	10.7	69.5	24.09	27.10
Ter 12	13.82 ± 0.17	-5.88	3.13 ± 0.79	18.0	74.5	24.22	26.18
Ton 2	11.66 ± 0.11	-6.21	2.83 ± 1.17	24.2	85.6	22.44	24.20
Whiting 1	14.61 ± 0.12	-4.23	0.43 ± 0.10	9.8	55.2	23.01	26.80